

Article

Determining Firebrand Generation Rate Using Physics-Based Modelling from Experimental Studies through Inverse Analysis

Amila Wickramasinghe, Nazmul Khan  and Khalid Moinuddin * 

Institute for Sustainable Industries and Livable Cities, Victoria University, Melbourne, VIC 3030, Australia; p.wickramasinghe@live.vu.edu.au (A.W.); nazmul.khan@vu.edu.au (N.K.)

* Correspondence: khalid.moinuddin@vu.edu.au

Abstract: Firebrand spotting is a potential threat to people and infrastructure, which is difficult to predict and becomes more significant when the size of a fire and intensity increases. To conduct realistic physics-based modeling with firebrand transport, the firebrand generation data such as numbers, size, and shape of the firebrands are needed. Broadly, the firebrand generation depends on atmospheric conditions, wind velocity and vegetation species. However, there is no experimental study that has considered all these factors although they are available separately in some experimental studies. Moreover, the experimental studies have firebrand collection data, not generation data. In this study, we have conducted a series of physics-based simulations on a trial-and-error basis to reproduce the experimental collection data, which is called an inverse analysis. Once the generation data was determined from the simulation, we applied the interpolation technique to calibrate the effects of wind velocity, relative humidity, and vegetation species. First, we simulated Douglas-fir (*Pseudotsuga menziesii*) tree-burning and quantified firebrand generation against the tree burning experiment conducted at the National Institute of Standards and Technology (NIST). Then, we applied the same technique to a prescribed forest fire experiment conducted in the Pinelands National Reserve (PNR) of New Jersey, the USA. The simulations were conducted with the experimental data of fuel load, humidity, temperature, and wind velocity to ensure that the field conditions are replicated in the experiments. The firebrand generation rate was found to be 3.22 pcs/MW/s (pcs-number of firebrands pieces) from the single tree burning and 4.18 pcs/MW/s in the forest fire model. This finding was complemented with the effects of wind, vegetation type, and fuel moisture content to quantify the firebrand generation rate.

Keywords: physics-based modeling; wildland fire; firebrands; FDS; wildland-urban interface



Citation: Wickramasinghe, A.; Khan, N.; Moinuddin, K. Determining Firebrand Generation Rate Using Physics-Based Modelling from Experimental Studies through Inverse Analysis. *Fire* **2022**, *5*, 6. <https://doi.org/10.3390/fire5010006>

Academic Editor: Maryam Ghodrat

Received: 29 November 2021

Accepted: 5 January 2022

Published: 8 January 2022

Publisher's Note: MDPI stays neutral with regard to jurisdictional claims in published maps and institutional affiliations.



Copyright: © 2022 by the authors. Licensee MDPI, Basel, Switzerland. This article is an open access article distributed under the terms and conditions of the Creative Commons Attribution (CC BY) license (<https://creativecommons.org/licenses/by/4.0/>).

1. Introduction

The hazard of wildfire on structures in the Wildland–Urban Interface (WUI) can be classified into direct flame contact, radiant heat, firebrand attack, and a combination of two or all of them [1]. Arguably, firebrands are the most devastating components of wildfires as they have the potential to initiate spot fires far from the fire front [2]. Post-fire investigations of the Pedoagao Grande fire (Portugal) [3] and Witch–Guejito fire (USA) [4] shows more than 50% of houses destroyed by the wildfires are from firebrands. Leonard et al. [5] reveals that firebrands caused ignition over 90% of houses in Australia during wildfire events.

The prediction of firebrands spotting has limitations due to the lack of knowledge of key processes of firebrand study: firebrand generation, transport, and ignition. Out of them, the firebrand generation has a significant knowledge gap compared to others as investigating particular aspect on the field scale is required higher safety precautions, advanced instruments and large financial resources. However, the firebrand generation rate is a demanding component to establish a complete integrated system to predict the wildfire risk in the operational context [6].

Physics-based modeling can be a viable alternative to experimental studies to study the firebrand transport and ignition. However, such modeling needs a set of thermophysical properties from experiments of various scales and data about firebrand size, shape, number, or mass of the collection, etc. Numerous experiments (both laboratory and field-scale) have been conducted to understand the firebrand characteristics, morphologies, ignition propensity and landing distribution to use in physics-based models [6–9]. The findings of these experiments reveal the effects of vegetation types, fuel moisture contents wind velocities, the intensity of fires for the firebrand generation and their physical properties [6,7,9,10].

Fuel moisture content (FMC) can severely influence the burning of vegetation and the characteristics of firebrands including generation rate. According to the tree burning experiments of Manzello et al. [9,11], the intensive burnings occurred with decreasing the FMC and the number of firebrands generation has increased. The geometry of firebrands was roughly cylindrical for all the experiments [9] performed and the mass distribution of firebrands shows a similarity for different tree heights in similar FMC levels [9].

Collecting firebrands from wildfires is a technique to understand the relationships between the nature of the fire and firebrand landing flux. For instance, several prescribed fire experiments were conducted in Pineland National Reserve (PNR) in the USA to measure the fuel properties, firebrand properties (velocity, size, number, mass distribution etc.), and fire spreading by Filkov et al. and El Houssami et al. [8,12,13]. They have recorded location-specific firebrand fluxes of 0.82–1.36 pcs/m²/s for the average fire intensity of 7.35–12.59 MW/m. This observation inferred that higher firebrand landing flux correlates with the higher magnitude of the fire and vice versa.

Investigating the size of the firebrands, number flux and the propensity to ignite spot fires for various fuel species was the focus of tree burning experiments of Hudson et al. [6]. Instead of conventional water-filled trays or plastic sheets to collect firebrands, they used fire-resistant fabrics to observe the hot firebrands (based on char marks). The highest average firebrand flux for a unit mass loss was recorded in the Douglas fir tree while the Grand Fir (*Abies grandis*) generated the highest hot firebrand flux. It shows the effect of fuel species for the number of firebrands generation. The area of the array of firebrand collection fabrics was increased and ignited relatively taller trees with comparable moisture contents by Adusumilli et al. [7] as an extension of the tree burning experiments of Hudson et al. [6]. Firebrands were collected from burning Douglas fir, ponderosa pine (*Pinus ponderosa*), and sagebrush (*Artemisia tridentata*) vegetations and linear extrapolation method was used to find the number of firebrands generated at the tree source. The results concluded that the total number of firebrands production increases with the height of tree/shrub and the hot firebrand number exponentially increase with decreasing moisture content of the vegetation species.

The tree burning and firebrand generation experiments of Bahrani et al. [14] investigated the effect of wind for firebrand generation for vegetation species of loblolly pine (*Pinus taeda*), Leyland cypress (*Cupressus leylandii*), saw palmetto (*Serenoa repens*), etc. The developed statistical model of this study shows the effect of wind speed for the number of firebrands generation for different fuel species. Outcomes of this experiment show that there is a linear relationship between mass and the projected area of the firebrands.

None of the above studies involving actual vegetation measured the rate of firebrand generation at the burning locations. Wadhwani et al. [15] carefully controlled the firebrand release rate and measured their initial velocities using the fire dragon experimental set-up. These were prescribed as input parameters in the respective physics-based model Fire Dynamic Simulator (FDS) to simulate firebrand transport and landing. By examining various drag models led to selecting the Haider and Levenspiel [16] drag model as it showed very good agreements between experimental and numerical landing distributions. It implies giving firebrand characteristics and generation data capable of accurately predicting the landing distribution by some physics-based models.

With the fidelity of the FDS, the current study presents a methodology to use FDS to determine the firebrand generation rate from the experimental firebrand landing distribution

data. This is done with a laboratory-scale single tree burning experiment as well as with field-scale multiple trees burning experiment. The firebrand landing distribution/collection data is reproduced by FDS by inputting the firebrand generation rate and initial velocities by trial and error. Hence, we term this process as the inverse analysis technique.

The specific objectives of this work are as follows:

1. To identify the firebrand generation rate of a single tree burning case.
2. To find out the firebrand generation rate of a forest (cluster of trees) burning.
3. To calibrate the firebrand generation rate as a function of wind, FMC, vegetation type.

Results from this study can be used in numerical modeling as firebrand generation rate inputs for simulating different severities/scales of wildfires. Further, the firebrand landing flux on houses in the wildland-urban interface (WUI) can be quantified to calculate the wildfire risk using physics-based modeling.

2. Methodology

2.1. Concept of the Inverse Analysis

Firebrand collection data are available from a single tree burning experiment [9] and a prescribed forest fire experiment [10]. The data consist of mass, sizes, shapes, and number of firebrands. However, there are no data available for the number of firebrands generated from burning vegetations of these experiments and the initial velocity or ejection direction of them. One of the main objectives of this work is to find the unknown firebrand generation rate as a function of the magnitude of the fire expressed in terms of heat release rate (HRR). To do that, we have conducted simulations with FDS injecting different firebrand numbers and their velocity and directions to reproduce the experimental landing number and mass distribution in a trial-and-error method. In doing so, we keep vegetation properties, heat release rates, wind velocity, and other environmental conditions same as the experiment. In each trial, we have calculated the firebrand landing numbers, mass, and flux at the collection points in the simulation domain. The simulation result of the firebrand collection is compared with the experimental collection. The inject number of firebrands in the following simulation is decided based on the surplus or shortage of the collection firebrand number. We continue this until the simulation and experimental firebrand collections closely match. When the matching occurred, then this is our base firebrand generation data that can be further refined taking account of other factors, such as wind velocity, vegetation species and relative humidity. We cite this process as the inverse analysis technique.

2.2. Governing Equations

FDS uses computational fluid dynamics multiphase modeling techniques to solve governing conservation equations for buoyant flow, combustion rate, energy, and species transport in a low Mach number approximation. The Large Eddy Simulation (LES) technique is used to account for the turbulences [17]. The filtered instantaneous continuity and momentum equations used in FDS are [17–19]:

$$\frac{\partial \bar{\rho}}{\partial t} + \frac{\partial \bar{\rho} \tilde{u}_i}{\partial x_i} = 0 \quad (1)$$

$$\frac{\partial \bar{\rho} \tilde{u}_i}{\partial t} + \frac{\partial}{\partial x_j} (\bar{\rho} \tilde{u}_i \tilde{u}_j) = - \frac{\partial \bar{P}}{\partial x_i} + \frac{\partial \bar{\Omega}_{ij}}{\partial x_i} - \frac{\partial \tau_{ij}^*}{\partial x_i} + \bar{\rho} g_i + f_b \quad (2)$$

where ρ , u , x , P , τ , g , f denote the density, velocity, coordinate, pressure, viscous stress, gravitational acceleration, and force term respectively. The i, j subscripts are direction indices and bar and tiled denote the Reynolds filter and Favre filtered quantities. FDS solves energy conservation by coupling the ideal gas law equation and the Poisson equation for pressure in the flow field. When the Navier–Stokes form resolves the velocity field, it is used the computed pressure term in the Poisson equation given below [17,18]:

$$\nabla^2 H = -\frac{\partial(\nabla \cdot \tilde{u})}{\partial t} - \nabla \cdot F \quad (3)$$

$$F = -\tilde{u} \times \omega - \bar{P} \cdot \nabla \left(\frac{1}{\bar{\rho}} \right) - \left(\frac{1}{\bar{\rho}} \right) [(\bar{\rho} - \rho_0)g + f_b + \nabla \cdot \tau_{ij}^*] \quad (4)$$

noting the stagnation energy per unit mass $H \equiv |u|^2 + \tilde{p}/\rho$, F is the momentum flux, ω is the vorticity, ρ is the instantaneous density and f_b is the external force vector excluding gravity. The pressure P , that spatially and temporally resolves for low-speed applications such as fire is decomposed into background pressure $\bar{p}(z, t)$ and perturbation $\tilde{p}(x, y, z, t)$ where only the background pressure retains in the ideal gas equation:

$$\frac{\bar{p}}{\bar{\rho}} = \frac{R}{W} \bar{T} \quad (5)$$

Here R is the gas constant and W is the molecular weight. The relationship of internal energy, e and enthalpy, h , is described in terms of thermodynamic (background) pressure: $h = e + \bar{p}/\rho$ to use in energy conservation equation [17] as below:

$$\frac{\partial}{\partial t} (\rho h_s) + \nabla \cdot (\rho h_s u) = \frac{D \bar{p}}{Dt} + \dot{q}''' + \dot{q}_b''' - \nabla \cdot \dot{Q}''' \quad (6)$$

where h_s is the sensible enthalpy, \dot{q}''' is the heat release rate per unit volume from chemical reactions and \dot{q}_b''' is the energy transferred to sub-grid-scale (SGS) particles. The conductive, radiative, and diffusive heat flux are represented by the term \dot{Q}''' . This term is computed by solving the heat transport equations. In FDS hydrodynamic solver guarantees that Equation (6) is satisfied for the energy conservation of the model. Fire is an inefficient combustion process of many fuel gases containing C, H and many other atoms that produce various products [17]. Tracking all the species is computationally expensive and FDS implements lumps species approach (a mixture of gas species transport together) to solve transport equations efficiently by reducing the number of equations. The species transport equation [17] that is solved in FDS given as:

$$\frac{\partial}{\partial t} (\rho Z_\alpha) + \nabla \cdot (\rho Z_\alpha u) = \nabla \cdot (\rho D_\alpha \nabla z_\alpha) + \dot{m}_\alpha''' + \dot{m}_{b,\alpha}''' \quad (7)$$

where Z is the mass fraction of α species, D is the diffusion coefficient, $\dot{m}_\alpha''', \dot{m}_{b,\alpha}'''$ source terms represent the additions of mass from evaporating droplets or other SGS particles such as vegetation and firebrands. FDS assumes the composition of gas in a cell space is either completely mixed or completely unmixed. At any point in time, the composition of a computational cell is determined by the mixed and unmixed portions as follows:

$$\tilde{Y}_\alpha(t) = \zeta(t) \tilde{Y}_\alpha^0(t) + (1 - \zeta(t)) \hat{Y}_\alpha(t) \quad (8)$$

where \tilde{Y}_α , \tilde{Y}_α^0 , \hat{Y}_α denote as cell mean mass fraction, initial cell mean mass fraction, and mass fraction of the species in the mixed reactor zone respectively. ζ is the unmixed fraction of mass within the cell. Time differential form of Equation (8) provides the solution of the chemical source term \dot{m}_α''' to use in the species equation (Equation (7)) as below.

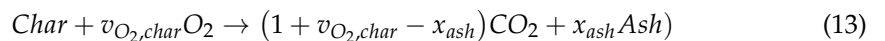
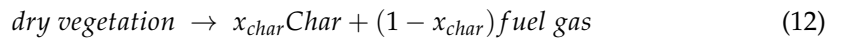
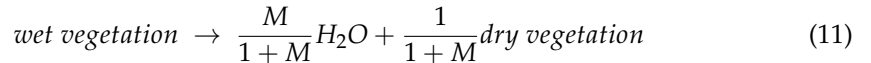
$$\dot{m}_\alpha''' = \rho \frac{d\tilde{Y}_\alpha}{dt} = \rho \left[\frac{\zeta}{\tau_{mix}} (\hat{Y}_\alpha - \tilde{Y}_\alpha^0) + (1 - \zeta) \frac{d\hat{Y}_\alpha}{dt} \right] \quad (9)$$

where, τ_{mix} is the mixing time. The heat release rate per unit volume \dot{q}''' depends on the combustion model. This quantity is fundamentally important in fire physics as it contributes significantly to the velocity divergence and heat transfer. In general, the total

heat release rate [17] is calculated as the summation of the products of \dot{m}_{α}''' (in Equation (9)) of each species and their heats of formation Δh , given as:

$$\dot{q}''' = - \sum \dot{m}_{\alpha}''' \cdot h_{\alpha}^0 \quad (10)$$

FDS consists of a special model for vegetation pyrolysis. The model contains three reactions to represent the solid phase thermal degradation for endothermic moisture evaporation (Equation (11)) [20], endothermic pyrolysis of dry vegetation (Equation (12)) [20], and exothermic char oxidization (Equation (13)) [20] as follows:



where M is the dry basis vegetation moisture content, x_{char} is the mass fraction of dry vegetation that is converted into char during pyrolysis. A significant amount of char oxidization only occurs at the vegetation material temperature is much higher than the temperature achieved in our simulations. Therefore, char oxidization is not accounted for below tree burning and forest fire modeling.

The Lagrangian particles are used in FDS to represent a wide variety of SGS objects (fuel particles, firebrands, etc.) along with their thermo-physical properties and geometric parameters [20]. They are introduced to the domain as stationary or dynamic particles. Vegetation is represented by stationary particles to randomly distribute through a given volume. In the current work, we specify the number of vegetation particles in a certain volume given by sextuplet in the form of N_PARTICLES and MASS_PER_VOLUME (kg/m³) [20]. The default shapes of the particles can be set as SPHERE, CUBE, and CYLINDER for both stationary and dynamic particles [20]. The firebrands are also introduced into the domain by a Lagrangian particle-based transport scheme to map their distribution and trajectories. This Lagrangian framework describes the physical variables for a solid element that passes through a flow where explained by the Eulerian framework to identify the location specified properties within the considering space [21]. Each Lagrangian particle interacts with the carrier fluid individually (two-way coupling). Due to this interaction (drag), a momentum loss of the particle is added to the fluid and vice versa. The total momentum f_b exchanged between Lagrangian particles and gas phase within a cell space is expressed as [17]:

$$f_b = \frac{1}{V} \sum \left[\frac{\rho}{2} C_d A_{p,c} (u_p - u) |u_p - u| - \frac{dm_p}{dt} (u_p - u) \right] \quad (14)$$

where, C_d is the drag coefficient, $A_{p,c}$ is the cross-sectional area of the particle, u_p is the particle velocity, m_p is the particle mass, and u is the gas velocity. The momentum transfer on the particle [17] results in acceleration which is given by:

$$\frac{du_p}{dt} = g - \frac{1}{2} \frac{\rho C_d A_{p,c}}{m_p} (u_p - u) |u_p - u| \quad (15)$$

The position of the particle can be determined by [17]:

$$\frac{dx_p}{dt} = u_p \quad (16)$$

The drag coefficient is a function of Reynolds number that is subjected to relative internal movement due to different fluid velocities. The default solution of the drag coefficient [17] in FDS is expressed for sphere particles where the Reynolds number Re is based on particle diameter D ,

$$C_d = \begin{cases} \frac{24}{Re_D} & Re_D < 1 \\ 24(0.85 + 0.15Re_D^{0.687}) & 1 < Re_D < 1000 \\ 0.44 & \end{cases} \quad (17)$$

$$Re_D = \frac{\rho |u_p - u| D}{\mu(T)} \quad (18)$$

denoting $\mu(T)$ is the dynamic viscosity of air at temperature T . Wadhwan et al. [15] found the Haider and Levenspiel drag model [16] showing good agreement for cylinder shape particles [15] of the short-range firebrand transport. In Haider and Levenspiel drag model, a few empirical correlations are accounted to represent the shapes of particles according to their sphericity. Therefore, the original FDS source code was modified including the Haider and Levenspiel drag model to use in the current simulations. The Haider and Levenspiel drag coefficient [16]:

$$C_{D,Ha} = \frac{24}{Re_D} \left(1 + A_{Ha} Re_D^{B_{Ha}} \right) + \frac{C_{Ha}}{1 + \frac{D_{Ha}}{Re_D}}, \quad Re_D < 2 \times 10^5 \quad (19)$$

where A_{Ha} , B_{Ha} , C_{Ha} , $D_{Ha} = f(\psi)$, are the empirical correlations expressed as a function of sphericity, ψ . The objective of applying the Haider and Levenspiel drag model is to replicate the drag forces acting on the firebrands and their movement with much realism and accuracy. The breakage of firebrands from vegetation is a complex combination of various parameters. Therefore, the mechanisms of firebrand production/tear-off are not investigated in this model.

2.3. Grid Convergence

Grid convergence is necessary for the accuracy of the simulation results. The objective of grid convergence study is to determine the appropriate grid resolution to capture the simulation results so that the results are free of discretization errors. However, a finer grid yields an asymptotically closer result to the final value at a high computational cost. The grid convergence index, GCI [22,23], provides a measure of convergence for the grid refinement studies, can be expressed as:

$$GCI = F_s \frac{\epsilon_{rms}}{r^q - 1} \times 100 \quad (20)$$

where, q is the numerical scheme order, hence the value is 2 for second-order scheme, F_s is the factor of safety. The recommended value of F_s is in the range of 1.25 to 3 [23], and r represents the grid refinement ratio that can be described as $r = (N_1/N_2)^{1/3}$, where N_1 and N_2 represent grid numbers from simulations with finer and coarser meshes, respectively. ϵ_{rms} is the rms value of the relative error that provides an initial measure of grid convergence for individual points. In this study, we have conducted the grid convergence study aiming to the higher reliability of results for different grid resolutions. The study is conducted for the parameters, such as mass loss rate, wind velocity and temperature.

2.4. Model Set Up

2.4.1. Single Tree Burning

A single tree burning is validated (pyrolysis and combustion) against Manzello et al. [9] burning experiment. The firebrand transport is also included together with this tree burning simulation to compare the collected firebrand mass and number with the experiment. The outcomes of firebrand generation rate, firebrand initial velocity and direction of this simulation are used as the initial input data for simulating a prescribed forest fire burning described in Section 2.4.2. In Manzello et al.'s laboratory experiment [9], an average of 70 firebrands from three similar Douglas fir tree burning experiments was collected, analyzed, and divided into classes to use as inputs to the single tree burning model

along with fuel load, thermo-physical properties of the vegetation and the initial burner details, etc. [9]. Thermo-physical parameters are taken from Moinuddin et al. [18], and Mell et al. [24] given in Table 1.

Table 1. Thermal parameters used in Douglas fir tree burning FDS model [18,24,25].

Parameters	Moisture	Vegetation	Char
Thermal conductivity (W/m K)	2.0	2.0	2.0
Specific heat capacity (kJ/kg K)	4.184	1.2	1.2
Density (kg/m ³)	1000	514	300
Reference temperature (°C)	100	200	-
Reference rate	0.002	0.0005	-
Heating rate (°C/min)	1.6	1.6	-
Heat of reaction (kJ/kg)	2500	418	-
Mass fraction	0.1	0.9	-

The tree geometry was taken as a cone shape having a height of 2.6 m and girth of 1.5 m same as the original tree. The area of the domain was determined according to the total area needed to set up FDS devices to represent the firebrand collection trays. The domain height was taken sufficiently high enough to capture the complete flame. The simulation domain of 8 × 8 × 10 m size was determined for the single tree burning model, which captures all the features of both fires and firebrands. The grid size was determined according to a grid convergence analysis as explained in the Section 3.1

A snapshot of Smokeview (FDS companion visualizing software) [26] is shown in Figure 1a with X and Z dimensions of the domain. The tree base is located at (0, 0) coordinate of the XY plane. The base height of the tree is 0.15 m relative to the horizontal plane and the circular shape burner of 30 kW heat release rate was prescribed around the tree base to be identical to the laboratory experiment. The location of firebrand collection trays is shown in Figure 1b. The individual size (30 × 50 cm) and the arrangements of FDS devices to record firebrand mass collection were the same as the experimental set-up.

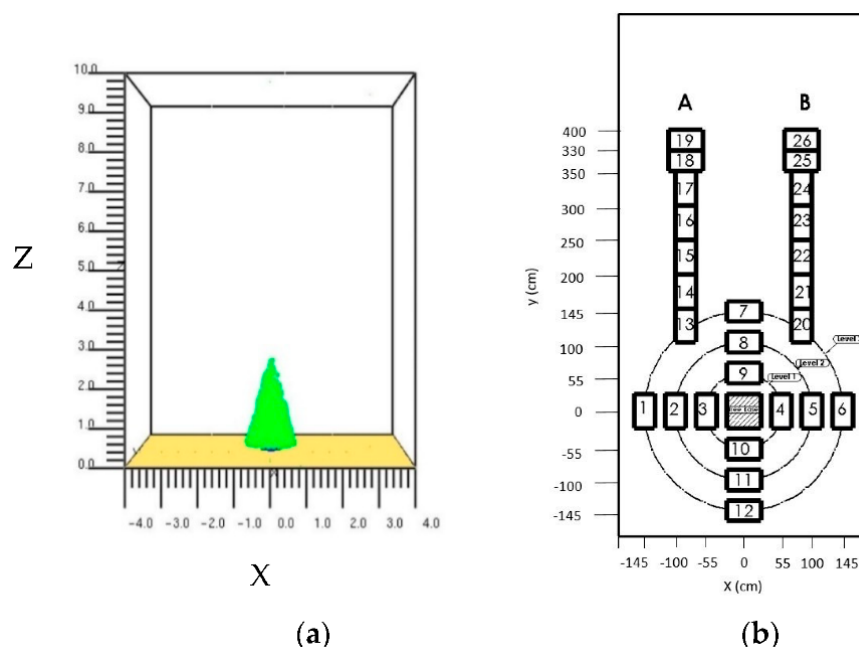


Figure 1. (a) Smokeview snapshot of the model tree (at 0 s time). (b) Plan view of the firebrand collection tray arrangement. Each tray is numbered 1 to 26 and the tree base is at the middle of 3–4 and 9–10 trays. A, B are the parallel branches of the tray arrangement. The trays are categorized into three levels presented as circles where the level 1 is the closest to tree base and level 3 is the farthest.

The burnable mass of the original tree consisted of needles and two different types of twigs [11]. The diameters and mass fractions of the fuel elements measured in the laboratory experiment are presented in Table 2. Mass Per Unit Volume (MPV) input parameter to the model was calculated by dividing the individual component mass by a total tree volume of 1.532 m^3 . The length of cylindrical shape burnable fuel particles was taken as 0.1 m [25]. The dry basis moisture content of the fuel was taken as 10% the equivalent to the experiment. The burner was activated for 15 s to provide a 30 kW HRR to start a sustained ignition.

Table 2. Composition and physical properties of burnable fuel of Douglas fir tree measured at NIST [27].

Fuel	Diameter (mm)	Mass Fraction (%)	MPV (kg/m^3)
Needles	0–6	65	4.208
Twigs (type 1)	0–6	17.5	1.133
Twigs (type 2)	6–10	17.5	1.133

As mentioned earlier, the firebrand generation rate, generation number or mass are not available from the tree burning experiment. Rather, the total number of collected firebrands on the collection trays, individual mass, and the dimensions of the firebrands are available. We classified these available firebrand data into 30 groups according to their mass ranging from 0.005 to 2.00 g. The numbers of firebrands falling into each mass class are known. The number of firebrands in each class and the diameter and length of the firebrands are shown in Figure 2a,b with varying mass. Out of the total number of collected firebrands, 97% were less than 1 g. The number of collected firebrands are decreased with the mass. The highest number of firebrands (27 pieces) are in the 0.02 g mass class. There are 60% of firebrands having a length of less than 50 mm and a diameter of less than 3.7 mm. The maximum firebrand length and diameter are 140 and 7.4 mm respectively. The shape, dimensions, and number of firebrands in each mass class were used as input parameters in this tree burning model.

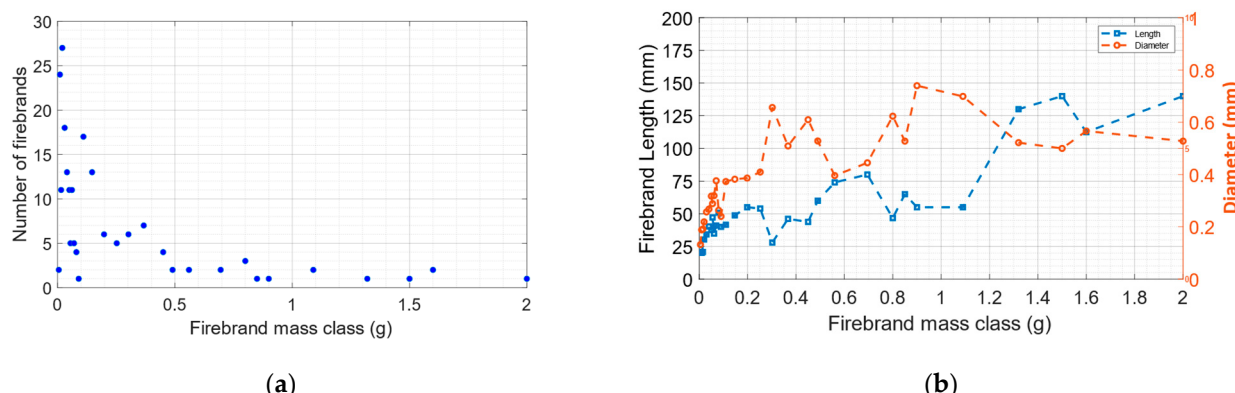


Figure 2. (a) Number of firebrands in each mass class (30). The collected number of firebrands are decreasing with increasing mass. The length and diameter of firebrands' show an increasing trend with the mass classes in (b).

In the laboratory experiment, the burning tree weight has become almost constant after 30 s implying that fuel burning and firebrand production has ceased [27]. To match with this, firebrand releasing was also maintained for 30 s in the simulation. Total simulation time was set to 45 s to provide adequate time to burn vegetative fuel and land the released firebrands on the ground or collection devices. The number of firebrands generated from the tree volume was controlled according to the HRR pattern of the burning. In other words, it is correlated to the mass loss rate due to the pyrolysis of the vegetation as given in Equations (7)–(9). We could reasonably assume a higher number of firebrands

released during the intensive burning (or intensive MLR) [28] period and vice versa. This assumption is strengthened by combining the results of the tree burning experiments conducted by Baker et al. [29] and Manzello et al. [9] as higher HRR results in higher firebrand production. Figure 3 illustrates the number of firebrands initiated in the tree volume as time evolves compared to the HRR at one of the trial cases.

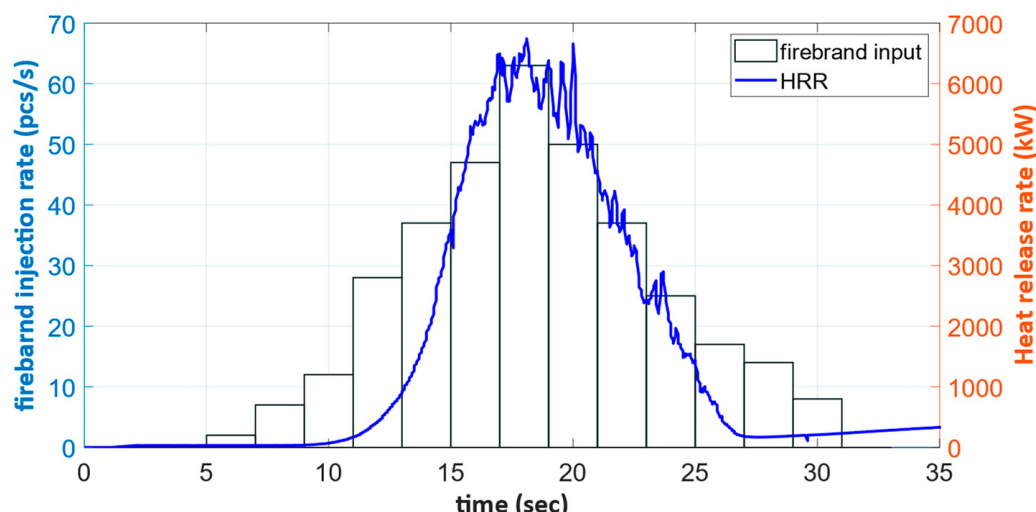


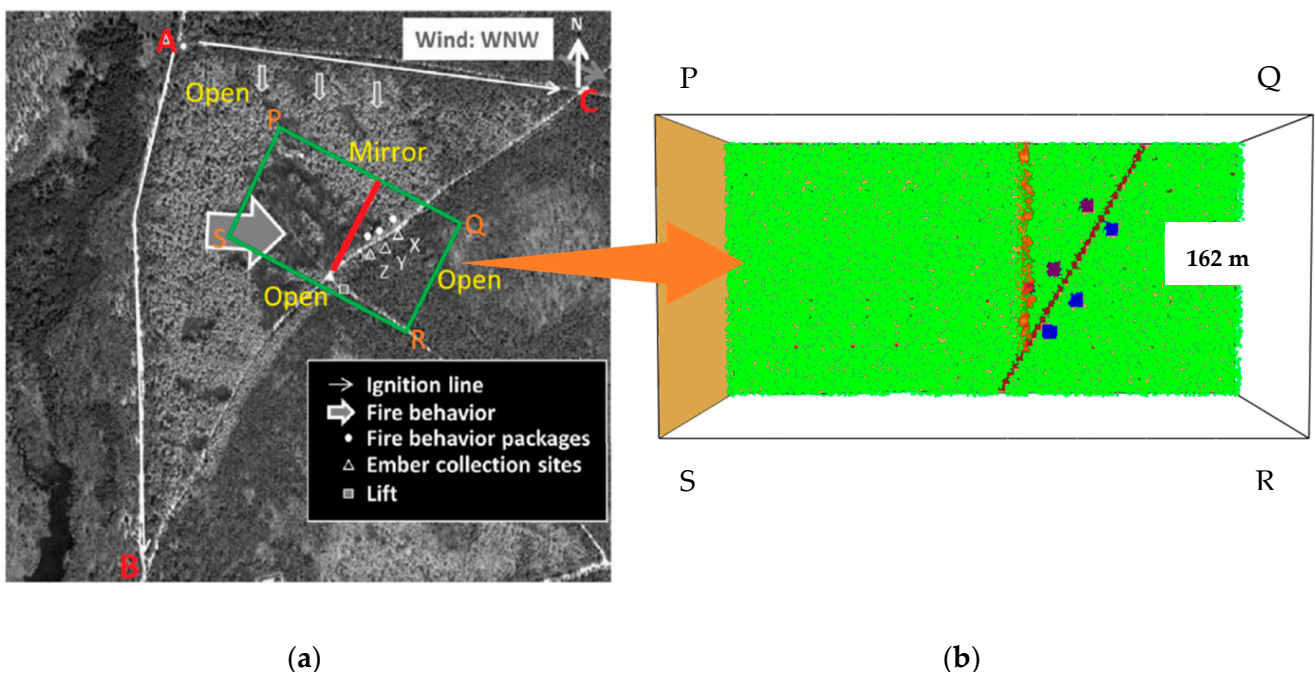
Figure 3. HRR of tree burning and the firebrand injection rate vs. time. The firebrand injection rate was adjusted according to the HRR.

Here the firebrand injection rate in every 2 s time interval is represented by the bar graph. The accumulation of firebrand injection rate over the time results the total number of firebrands produced during the tree burning. The first set of firebrands was initiated around 5 s when the flame appeared at the bottom of the tree. The firebrand generation pattern was synchronized with the HRR pattern as much as possible to fulfil the total generation number (a multiplication of the collected number of firebrands (70 pieces)) of firebrands. During the laboratory experiment, no wind was imposed on the burning tree [9] and the simulations were also conducted in absence of wind replicating the laboratory experiment.

The firebrands pyrolyzing was not accounted here assuming the time between firebrands initiating and landing is not sufficient for a significant pyrolyze and mass reduction of them. The firebrand burnout was also ignored to match with the experiment because they quenched as soon as landing on the water filled trays. The total mass of a particular firebrand type landed on a tray (FDS device) could be found at the end of the simulation. The number of firebrands was calculated by dividing the total mass by the individual mass of that firebrand class. As this continued for all the landed firebrand classes, we could calculate the total number of firebrands collected, the total mass and the number distribution of them. The grid convergence results, validation of mass loss data and inverse analysis of firebrand generation are presented in Section 3.1 for the single tree burning.

2.4.2. Multiple Trees (Forest) Burning

The multiple trees burning was set up following the prescribed forest fire experiment conducted in Pinelands National Reserve (PNR), New Jersey, USA in 2016 [28]. The main objective of this simulation is to obtain the firebrand generation rate of a forest fire. Figure 4a shows a satellite image of the post-burn triangular shape forest area where the dominant fire swept inward to AB road with an alignment to the wind flow. The diagonal of the region (BC) is a 3 m wide dirt road acting as a fire break separating the X, Y, Z Fire Behavior Packages (FBP) and Firebrand Collection Centers (FCS).



(a)

(b)

Figure 4. (a) A post-fire satellite image of the PNR burning plot [28]. The X, Y, Z Firebrand Collection Sites (FCS) are located at the right side of the dirt road. Fire Behavior Packages (FBP) are established on the left side of the dirt road opposite to the FCSs. The wind direction is WNW. The focused area for modeling is marked in a green color rectangle (not to the scale). The red color line is the fireline location at a certain time. (b) Snapshot of Smokeview of the focused area of the FDS modeling including the major locations of the burning site.

Simulating the complete burning plot (28 ha) is not feasible in terms of computational cost, so the PQRS area (336×162 m) was determined as the simulation domain including the critical points of FCS, FBP, meteorological station and fire break. The fireline was defined to prescribe as a stationary line. The most reasonable location of the fireline was found with the available experimental data of Fire Rate of Spread (ROS), firebrands arrival time to FBPs, time durations of firebrand showers on the firebrand collection sites and, the distances between FCSs and FBPs. The calculated fireline location was laid at the area where the highest canopy fuel consumption occurred (Figure 4a: correspond to the dark color area in the PQRS boundary). The shortest distance to the fireline is 16.16, 33.61 and 56.83 m from the Z, Y, X firebrand collection centers respectively. The fire intensity of the fireline was chosen as 18.46 MW/m based on the upper limit of average fire intensity at the highest consumption of canopy fuel in the field experiment. The depth of the fireline is not directly available from the experiment and it was calculated according to Alexander et al. [30], that the depth (D) is expressed by:

$$D = ROS \times T_r \quad (21)$$

where T_r is the residence time found as 24 s with the difference of the arrival and the departure time of the fire to FBP Z. The average ROS from the experiment is 0.289 m/s and the fireline depth was calculated as 7 m. The heat release rate per unit area (HRRPUA) of the fireline was determined as 2637 kW/m^2 , dividing the fire intensity ($18,460 \text{ kW/m}$) by the fireline depth to use as an input parameter in the FDS input file. The length of the fireline (130 m), was determined as the distance between the fire break and the PQ boundary of the domain. Due to computational cost and lack of thermal degradation and flammability data, we are prescribing fire rather than simulating the burning process like the single tree case.

The contacting boundary PQ to the fireline was set to a 'MIRROR' boundary condition (free slip) to replicate the extending nature of the fireline beyond the boundary. The opposite

boundary SR, domain top, and downstream boundary RQ were set to ‘OPEN’ boundary condition while a wall of wind was prescribed assigning to the exterior lateral boundary PS to maintain the ‘ATMOSPHERIC’ flow profile. The number of eddies at the inlet was calculated and added according to Jarrin et al. [31]. The domain surface is covered with 1 m thick understory layer. The average height of the canopy was taken as 18 m from the estimation of experimental LiDAR measurements [28] and thickness of it is about 9 m. Both understory and canopy start from the PS inlet and spread towards the downstream boundary as in Figure 4b. The non-burning cylindrical shape vegetation particles (needles and twigs) in the canopy and understory volumes have their own drag laws defined according to the shapes to account for the drag forces. The tree trunks are modelled as 12 m height non-burning obstacles randomly situated within the modelled forest. The ambient temperature of 13 °C and mean relative humidity of 22% were maintained in the simulations to reproduce the environmental conditions of the field experiment. Table 3 shows the vegetative fuel dimensions, thermo-physical properties, FMC, mass per volume of the dominant fuel Pitch Pine (*Pinus rigida* Mill.) of PNR as per Muller et al. [32], Filkov et al. [28], and Ioannis et al. [33].

Table 3. Thermo-physical parameters and fuel loads are used in the simulation [28,33,34].

Parameter	Moisture	Needles	Twigs
Thermal conductivity (W/m K)	2.0	0.1744	0.1737
Specific heat capacity (kJ/kg K)	4.184	1.691	1.610
Density (kg/m ³)	1000	787	512
Thickness (m)	-	0.003175	0.0015
Length (m)	-	0.1	0.1
Geometry	-	Cylinder	Cylinder
Moisture content (Wet basis %)	100	55	24
Mass per volume (kg/m ³)	-	0.2915	0.1783

The FCS and FBP were set up according to the distances given in the field experiment. The area (10 × 10 m) of each kept without vegetation to facilitate smooth firebrand landing avoiding any interruption of the dense canopy or the understory. The temperature and the flow velocity devices were set at the center of the FBPs to capture data to compare with the experiment. The firebrand collection trays of the experiment were replicated by setting FDS devices at FCSs to capture the total mass of each type of firebrand landed in a certain time.

In Figure 5, the images show 42 types of firebrands that were collected from a similar prescribed burning conducted nearby forest area (Pine Barrens, NJ, USA) in 2013 [8] as a part of this experiment series. These images were converted into greyscale with a threshold level of 0.67 and analyzed in MATLAB to obtain eccentricity to determine the shape (sphere, cylinder, cube) and dimensions (length, width, diameter). The data of these 42 types of firebrands were used as inputs in the model while varying their generation numbers based on the composition of the experimental firebrand collection. Most of these firebrands are fragments of barks (81%) and the rest of them are twigs (9.5%) and needles (9.5%). Out of them, 55% are cylinders, 32.5% are cubic and 17.5% are sphere shape firebrands. The thermophysical properties were taken the same as the vegetative fuel for these particles. The density variations of the firebrands due to moisture evaporation, pyrolysis and burning were estimated according to Menzemer et al. [35].

It is important to have a steady wind field before starting the fire or generating firebrands from the fire. The next attempt was to obtain a developed wind field having an average wind velocity of 2 m/s to match with the experimental wind flow. In the experiment, wind speed was recorded at a 17 m height anemometer close to the firebrand collection area. The driving wind flow, u was prescribed at height of z as the power-law atmospheric wind profile with 1/7th exponent expressed as [20]:

$$u = u_0 \left(\frac{z}{z_0} \right)^p \quad (22)$$

where u_0 is the reference velocity at the inlet, z_0 is the height of the referenced wind speed, and p is the exponent which is $1/7$. A few trials were carried out with several initial velocities at the PS inlet boundary to obtain the intended average wind velocity at the anemometer location. The simulations were run around $5 \times$ domain travel time (DTT) to have a fully developed wind profile. The developed wind field was used as a precursor to obtain a steady wind field in a shorter time in following trials.

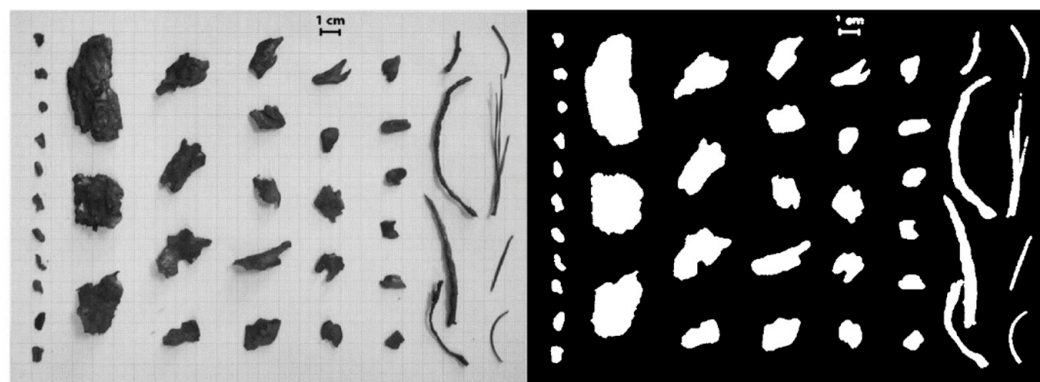


Figure 5. Image of different sizes and shapes of firebrands collected in El Houssami et al. [10] (**left**), and a greyscale conversion by MATLAB (**right**). Barks, twigs, and needles were collected as firebrands in this experiment.

Once the wind profile was obtained, the fire was prescribed and continued for 10 s to avoid the effect of initial shock on the flow by the sudden heat release. When the flow became steady, firebrands were started to inject over the volume of the fireline. This volume consists of the fuel particles of the canopy and the firebrands were initiated randomly through the volume among the fuel particles.

The firebrand generation data, such as the initial velocity, directions, generation rate were taken from the single tree burning simulation. The advantage of using single tree burning data is to include a reliable starting point for the inverse analysis, which reduces the number of trials needed to optimize the forest model. The total number of firebrands generation rate was calculated based on the prescribed fire (18.46 MW/m), length of the fireline (130 m), and the number of generation rate that was found in Douglas fir tree burning simulation in Section 3.1.2.

The total firebrand generation number is the summation of the individual particles of each firebrand size class. In the experimental firebrand collection, the firebrands are divided into 6 size classes as $0.75\text{--}5$, $5\text{--}10$, $10\text{--}20$, $20\text{--}30$, $30\text{--}50$, $>50 \times 10^{-5} \text{ m}^2$ based on their projected area and the percentage of them in each size class are known. These percentage numbers were maintained in the firebrand injecting batches of the simulation too. The grid convergence results, inverse analysis, and the firebrand generation rate as a function of HRR are presented in detail in Section 3.2 for the prescribed forest fire modeling.

3. Results and Discussion

3.1. Validation of Mass Loss Data and Inverse Analysis on Firebrand Generation-Single Tree Burning

The grid convergence study was conducted for the single tree simulations using grid resolution of 100, 75, 50 and 37.5 mm to determine the converged grid size. The results of mass loss rate (MLR) and heat release rate (HRR) were compared for different grid sizes as shown in Figure 6a,b, respectively. It is found that MLR profiles are almost similar except 100 mm grid case, where there are some variations of peak MLR values. However, the HRR results are showing some noises at peak values and there is a gradual convergence of HRR values with decreasing grid sizes.

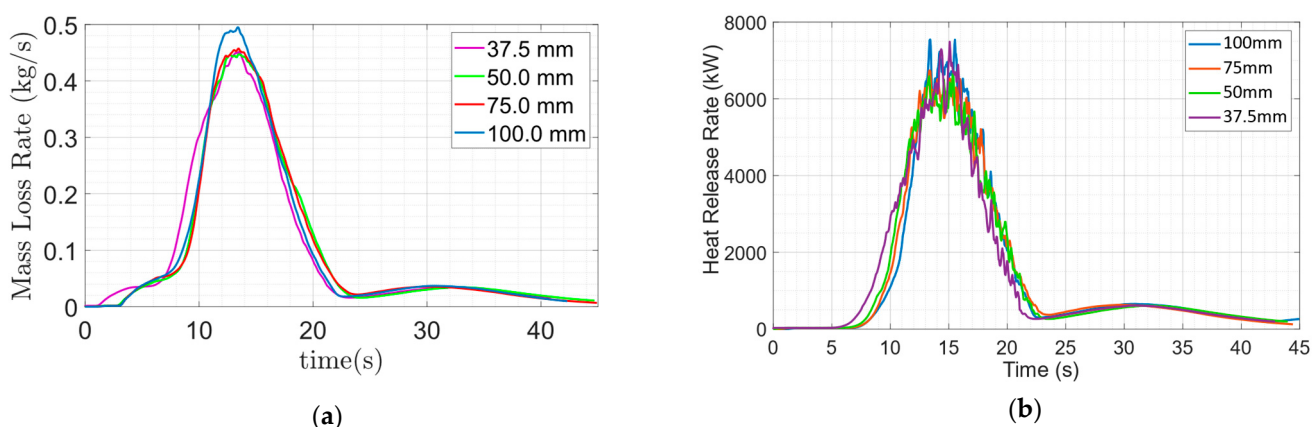


Figure 6. Comparison of peak aligned (a) MLR, (b) HRR for 2.6 m Douglas fir tree simulations for grid size 100, 75, 50 and 37.5 mm.

The grid convergence was further examined by GCI during the intensive burning period of 15 to 20 s in terms of MLR. The analysis was done for a particular grid size against the adjacent smaller grid size. As it is a laboratory scale experiment, F_s is taken as 3. The peak-to-peak MLR difference was also calculated for each case. The results of these comparisons are presented in Table 4.

Table 4. Grid convergence and peak-to-peak mass loss rates percentage difference.

Grid	GCI (%)	% of Peak-to-Peak MLR
100 mm/75 mm	28.5	12.9
75 mm/50 mm	4.0	3.18
50 mm/37.5 mm	10.8	0.26

The highest GCI is obtained by 100 mm/75 mm grids and the minimum is 75 mm/50 mm grids. The GCI of 50 mm/37.5 mm is in between them. Although the peak-to-peak MLR differences do not show the same trend, the percentage differences of 75 mm/50 mm and 50 mm/37.5 mm are less than 4%. The FDS' particle model was also examined for these grid sizes in terms of firebrand landing mass distribution and obtained a -6% to +5% difference for 100–37.5 mm grids compared to the 50 mm grid. According to GCI, peak MLR differences, and firebrand mass distribution differences, 50 mm grid size was selected as reasonable to use for further simulations considering the fidelity of the results convergence and the computational cost.

3.1.1. Validation of Mass Loss Data

In the NIST laboratory experiment [9], the tree was placed on load cells to record its weight as the burning process continued. The experimental MLR was calculated to compare with the simulation. The comparison in Figure 7 shows the shapes of these MLR profiles of the experiment and simulation are qualitatively similar. The difference in the total mass loss throughout the time is only 8.5%. The peak mass loss rate of the experiment is 0.417 kg/s whereas the simulation shows an overestimate of 0.447 kg/s which is only a 6.7% difference.

The HRR affects the flow behavior around the burning tree by forming a fire-induced buoyancy. The pressure from this flow exerts the drag force on the firebrands released from the tree to determine the resultant force on them and their dynamics. Having a similar flow profile in the tree burning model is important to approximate the movements of firebrands reasonably similar to the experiment. However, HRR data are not available from the laboratory experiment. Instead of that we can use the validated MLR to assume that the HRR of the experiment as HRR is the product of MLR and heat of reaction (HoR) as per

Equation (10). Therefore, we can assume the present mass loss data validation ensures the flow behavior around the model tree replicates the experiment.

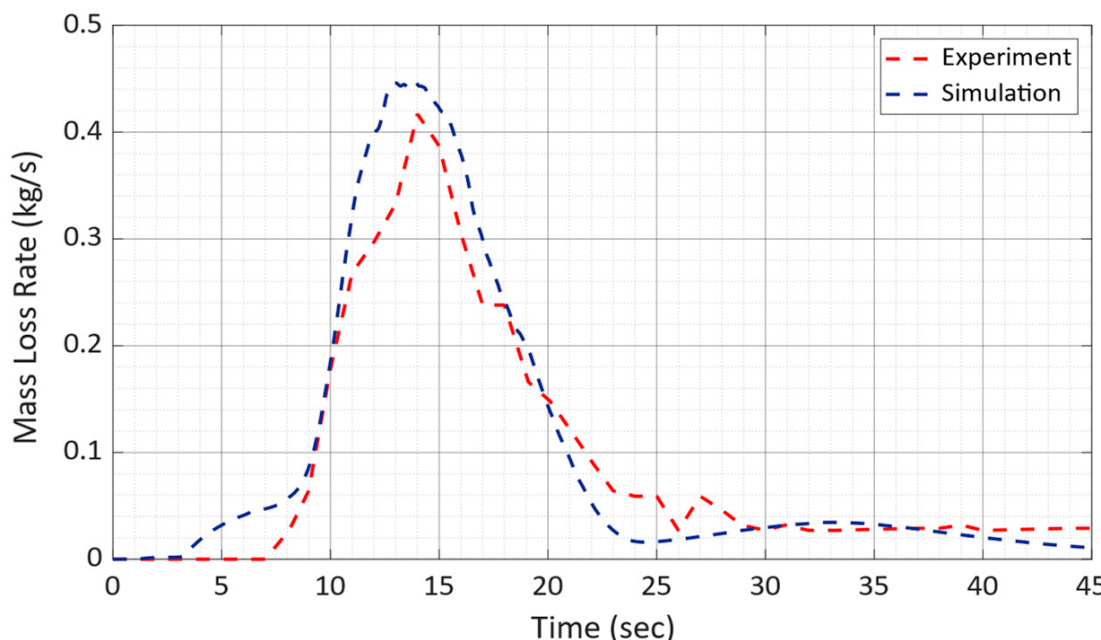


Figure 7. MLR comparison of experiment and FDS simulation using 50 mm grid. The shapes of the two curves are reasonably similar. Simulation results show higher total mass loss than the experiment during the simulation time of 45 s.

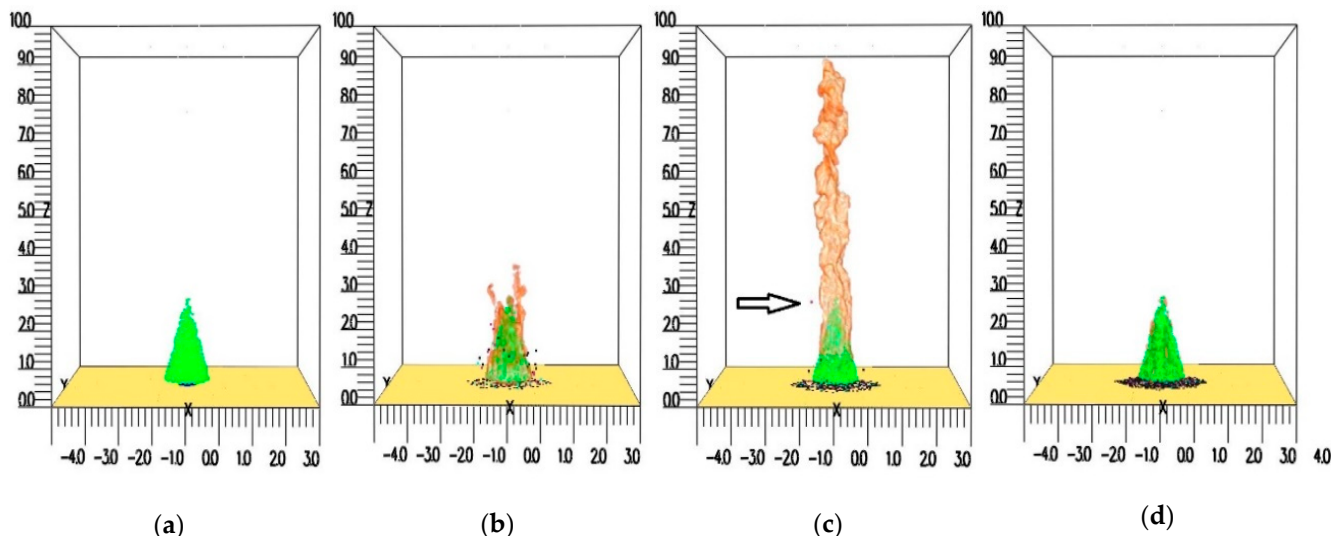
3.1.2. Finding Firebrand Generation from Single Burning Tree by Inverse Analysis

We set up the single tree case with the firebrand generation number, mass and velocities as shown in Table 5. First, the firebrands were injected at different initial velocities to reach the collection devices at 1, 2, 3 levels and A, B parallel branches (shown in Figure 1b) under the influence of gravity and fire buoyancy. In simulation 1, the smaller initial velocities were not sufficient to transport firebrands towards the distant collection trays. Most of them landed on the trays nearby the tree base. Increasing velocities showed some of firebrands landing on the distant trays in the following trials. Horizontal and radial velocities of 70 cm/s and 210 cm/s are the minimum velocity components that could obtain significant number of firebrands on all levels of trays including A, B parallel branches under the effect of convective column and gravity. Subsequently, the same procedure was carried out by varying the injected number of firebrands as in simulations 2, 3 to find whether there is a significant number of firebrands reaching to the collection devices under different initial velocities. Irrespectively to the injected number of firebrands, the minimum velocities to reach adequate number of firebrands were found as 70 cm/s and 210 cm/s even in simulations 2 and 3. This velocity (and direction) was set as the firebrand initial velocity input parameter for the following series of simulations. Figure 8 represents the Smokeview visual outputs of tree burning at different times and firebrand distribution with 70 cm/s and 210 cm/s initial velocities.

Next, the firebrand generation number was varied to map with the experimental results both in terms of the collected firebrand number and the total mass. The total injected number of firebrands were maintained as a factor of the collected number of firebrands of 70 pieces as shown in Table 6. In every multiplication, the landed number of firebrands and the total mass were compared with the experiment and if the result is less than the experiment, succeeding higher multiplication was applied. This process was continued until the simulation and the experimental results were satisfactorily matched.

Table 5. Number, velocity, and direction of firebrand variations to obtain matching collection.

Case	Generated/Injected Firebrands		Velocity and Directions	
	Number	Mass(g)	Vertical (cm/s)	Radial (cm/s)
Laboratory experiment	unknown	unknown	unknown	unknown
Simulation 1 (50 mm grid)	2 × 70	23.23	5	0
			10	30
			60	180
			70	210
Simulation 2 (50 mm grid)	3 × 70	34.85	5	0
			10	30
			60	180
			70	210
Simulation 3 (50 mm grid)	4 × 70	66.80	5	0
			10	30
			60	180
			70	210

**Figure 8.** Snapshots of Douglas fir tree burning and firebrand distribution at: (a) zero seconds; (b) 14 s; (c) 21 s; (d) 35 s. The arrow in (c) shows some firebrands moving upwards with the convective column during the intensive burning before landing on the floor.**Table 6.** Mass received by trays injecting a different number of firebrands.

Case	Number of Firebrands		Mass of Firebrands (g)		Firebrands Receiving Trays
	Injected	Collected	Injected	Collected	
1	70 × 4	66	66.80	16.45	1 to 12, 13 and 14
2	70 × 5	79	86.92	18.90	1 to 12, 13 and 14
3	70 × 6	106	99.40	26.36	1 to 12, 13 and 14

Table 6 presents the results of some simulation cases completed with different injected numbers and respective collected number of firebrands, injected and collected mass and, the numbers of trays that firebrands received. It shows that injecting 70 × 5 firebrands could obtain 18.90 g of firebrands in the trays (FDS devices), which is the closest result to the experiment both in terms of the total mass (18 g) and the number of firebrands (70 pieces).

The firebrand mass distribution contour map of case 2 is presented in Figure 9. The tree base is at $(0, 0)$ coordinate. According to the figure, the mass distribution of firebrands around the tree is not uniform. More firebrands have landed in the negative y -direction. This asymmetry distribution may be because of the random characteristics of fire-induced instant buoyancy and the resulting flow behavior around the tree. This generated random flow could affect the dynamics of the firebrands to move and land them asymmetrically on the collection devices. The maximum mass of firebrands obtained by a tray is around 4 g.

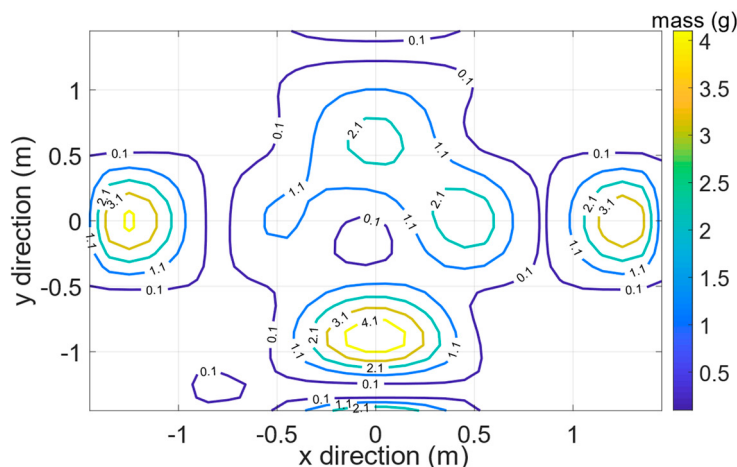


Figure 9. Contour map of firebrand mass distribution around the tree. The total inject number of firebrands is 5×70 . Tree is mounted at $(x, y) = 0, 0$. The figure shows firebrand distribution is not uniform and more particles have landed in the negative y -direction.

Once the experiment and simulation are closely matched, the average HRR was calculated based on the HRR data written in the FDS HRR output file. The firebrand generation rate was calculated by dividing the total number of injected firebrands by the average HRR and the duration of the firebrand injection. In case number 2, the total inject number of firebrands is 347 pieces and the average HRR is 3.596 MW where the burning and firebrand injecting proceeded for 30 s. Therefore, the calculated firebrand generation rate for the 2.6 m height Douglas fir tree with 10% FMC is 3.22 pcs/MW/s. The model validation of single tree burning, and the determination of firebrand generation rate led us to use the same inverse analysis technique to find the firebrand generation rate of the experimental forest fire.

3.2. Inverse Analysis of the Prescribed Burning Experiment with Pitch Pine Forest

3.2.1. Grid Convergence Analysis

Similar to the single tree burning simulations, the grid convergence was studied for the prescribed fire modeling. This was conducted in terms of time-averaged velocity, and time-averaged temperature. The grid sizes of 1000, 750 and 500 mm were used for simulations. The velocity data were taken before starting the fire and the temperature data were taken after starting the fire at the strategic locations ($x = 182$ m, 217 m and, 252 m) before and after the fireline with 35 m apart.

The time-averaged wind velocity profiles are presented in Figure 10a–c. These profiles show that the developed wind velocity profiles obtained using 500 and 750 mm grids are closer than that obtained using 1000 mm grid. There are some inflection points below 40 m due to the drag of the vegetation (understory, canopy and, near canopy area). In this region, the velocity profiles show a non-monotonous pattern of convergence at $x = 182$ and 217 m. The time-averaged temperature profiles are displayed in Figure 10d for the same locations.

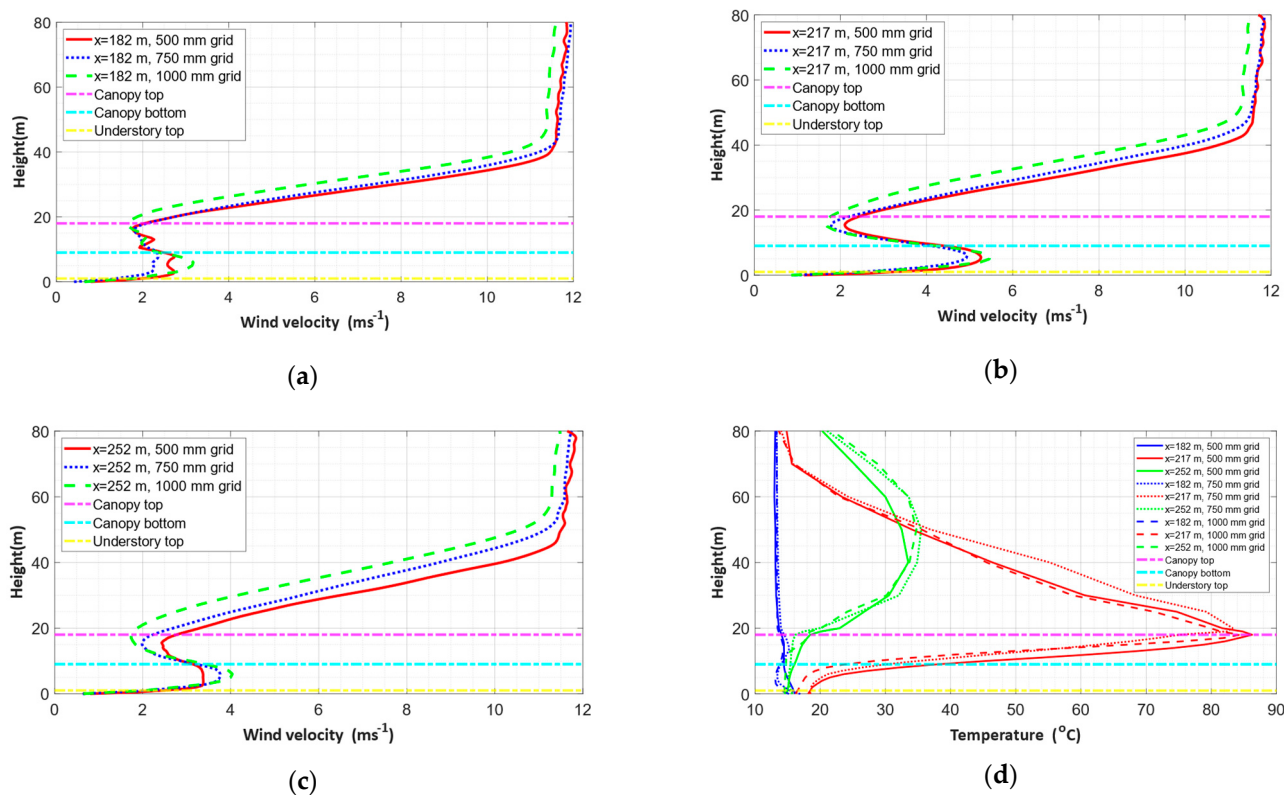


Figure 10. (a–c) The graphical comparison of time-averaged velocity and (d) time-averaged temperature for 500, 750 and, 1000 mm grid sizes at $x = 182$, 217 and 252 m.

The pattern of convergence for these temperature profiles is non-monotonous. The highest temperature values were recorded at $x = 217 \text{ m}$ followed by the temperature at $x = 252 \text{ m}$ and $x = 182 \text{ m}$. To quantify the grid convergence, the GCI was calculated for time-averaged velocity and temperature at the same locations and presented in Table 7. Because of the field scale simulations, F_s is taken as 1.25. The calculated GCIs are smaller for 500 mm/750 mm grids compared to 750 mm/1000 mm grids for both velocity and temperature at all the focused locations. The velocity GCIs of 500 mm/750 mm are less than 16% and maximum GCI of temperature is about 19%. Considering the GCI and graphical patterns, 750 mm grid was chosen as the appropriate grid size to use in the next simulations of the inverse analysis.

Table 7. Grid convergence of velocity and temperature.

Grid Sizes	GCI (%)					
	Velocity at			Temperature at		
	182 m	217 m	252 m	182 m	217 m	252 m
500 mm/750 mm	15.3	11.6	12.4	6.9	19.1	13.4
750 mm/1000 mm	31.7	21.3	22.9	8.1	26.5	15.2

Figure 11 shows the developed wind profiles at 750 mm grid at different longitudinal locations before the fireline. The wind profiles are reasonably collapsing each other from mid to top of the domain. However, there are inflection points at the subcanopy and immediately above the canopy region, which is expected due to wind field modification caused by canopy drag laws [36]. The canopy is 9–18 m thick (Z - direction) and the understory is 1 m where the wind flow shows the characteristics of velocity reduction because of the drag of the dense vegetation. The inlet velocity is 11.4 m/s at 2 m height.

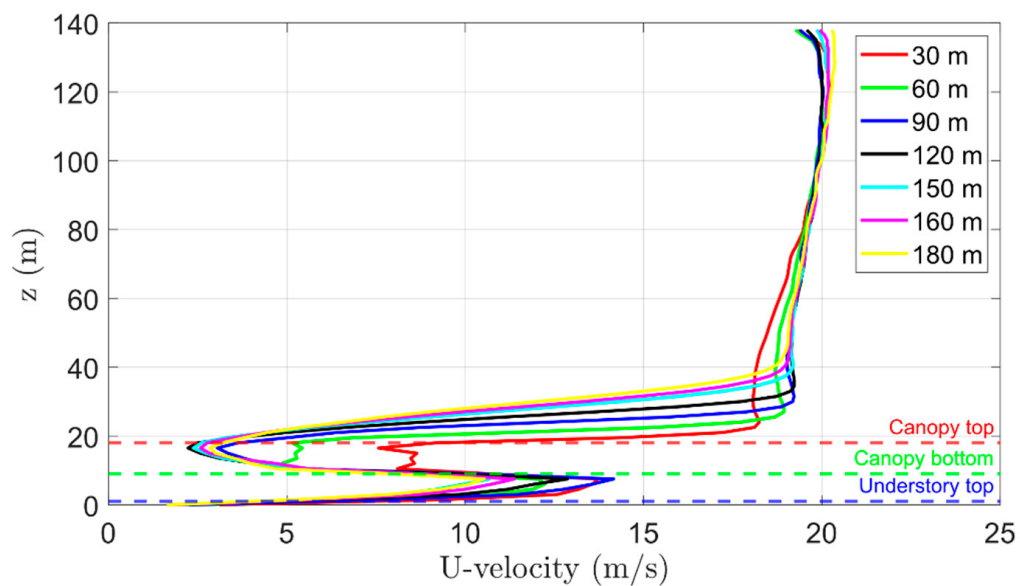


Figure 11. The developed wind field with the 750 mm grid is shown at different x locations from the inlet of the domain. The heights of the canopy and understory are also shown in dashed lines.

3.2.2. Finding Firebrand Generation Rate by Inverse Analysis

The fire was started after obtaining a developed wind field. Figure 12 is a Smokeview snapshot of the wind field and firebrands after starting the fire. Most of the firebrands were landed at the nearest collection center (Z) to the fireline. The number of firebrands landing decreases with the increase of distance between the fireline and the collection centers. The convective column has leaned towards the downwind direction because of the wind force.

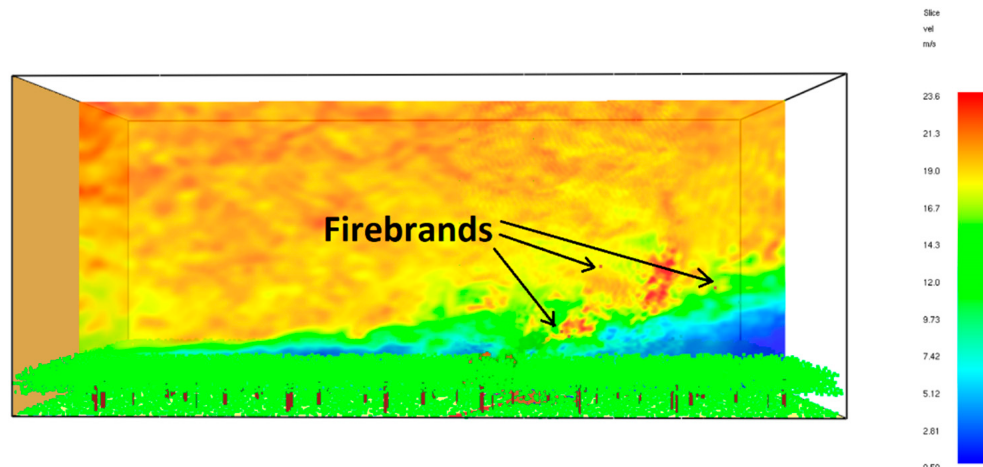


Figure 12. A snapshot of Smokeview of firebrand transporting with the effect of wind and fire buoyancy towards the area of firebrand collection centers. The velocity slice file at $Y = 0$ illustrates the developed flow with eddies. The arrows show some of the firebrand transport with the influence of the convective column and wind before they land. The visualizations of firebrands are not to the scale.

At the beginning of the trials, the number of firebrands reaching the furthest FCS X was significantly low. The initial firebrand velocity taken from single tree model was not sufficient to transport a significant number of particles toward the FCS X. To overcome this issue, the initial velocity of firebrands was adjusted based on trials. A few trials were carried out giving different combinations of horizontal and vertical velocities to reach firebrands sufficiently on collection sites.

The simulation was then conducted by varying the firebrand generation rate to match the experimental results in terms of the total number of collected firebrands, total firebrand flux, individual firebrand number and flux according to the size classes. The firebrand fluxes ($\text{pcs}/\text{m}^2/\text{s}$) on X, Y, Z locations were calculated by dividing the total number of firebrands landed, by the area of each collection site (100 m^2) and the period between the first and last arrival of firebrands. This process was continued for individual firebrand size classes too. These results were compared with the experiment at each firebrand collection site. Sometimes an increment or decrement of the number of firebrands in a certain firebrand class at a certain location affected the landing flux of another location at the succeeding run. Therefore, the adjustments were carried out carefully until satisfactorily match with the experimental results for all three collection sites. Table 8 shows some of the simulations carried out by tweaking the firebrand initial velocity, and the inject number in this inverse analysis process.

Table 8. Firebrand flux at Z, Y, X firebrand collection centers in a few trials of the inverse analysis.

Case	Wind Speed (m/s)	Firebrand			Flux ($\text{pcs}/\text{s}/\text{m}^2$)		
		Initial Velocity (m/s)	Injection Rate (pcs/s)		FCS Z	FCS Y	FCS X
TA	≈1.94	(4.2, 0.0, 2.1)	9881	2.105	1.562	0.074	
TB	≈2.02	(6.2, 0.0, 2.1)	9881	1.332	1.499	0.255	
TC	≈1.93	(8.3, 0.0, 2.1)	9042	1.218	1.120	0.522	
TD	≈1.89	(8.3, 0.0, 5.2)	9042	1.253	1.341	0.306	
TE	≈1.87	(8.3, 0.0, 6.2)	9042	1.154	1.196	0.271	
TF	≈1.95	(9.3, 0.0, 4.2)	8907	1.343	1.230	0.289	
TG	≈1.98	Varied on particles	9881	0.738	1.415	0.214	
TH	≈2.2	(8.3, 0.0, 2.1)	11,006	1.946	0.977	0.798	
TI	≈2.13	(8.3, 0.0, 2.1)	14,436	2.835	1.355	0.203	
TJ	≈2.17	(8.3, 0.0, 2.1)	12,367	1.625	1.170	0.641	
TK	≈2.13	(8.3, 0.0, 2.1)	11,171	1.375	1.082	0.870	
Experiment	2.0	NA	NA	1.361	0.902	0.824	

According to the results in Table 8, the TA case has a lower firebrand flux at the X location compared to the experiment. The fluxes on Z and Y locations are overestimated. These Z, Y collection centers are closer to the fireline than X. It could be assumed that firebrands do not have enough initial velocity to interact with wind and convective column to transport to a distant location. This might be the same reason for landing more firebrands at Z and Y collection sites. As the next step, the initial horizontal velocity was increased up to 6.2 m/s in the following TB case. This change resulted in landing more firebrands on X location compared to the TA case while Z, Y location's firebrand fluxes became closer to the experimental results than the previous overestimation. In the case of TC, the velocity was increased further, and it showed more landing flux at Z than in the case of TB. At this point, all the firebrand collection centers received a reasonable number of firebrands. However, increasing the firebrand velocity furthermore resulted in moving out a significant number of firebrands from the convective column and landing again more closely to the fireline. This behavior is shown in case TF. Hence the initial velocity increment of firebrands is limited to 8.3 m/s horizontal and 2.1 m/s vertical velocities to receive enough firebrands to all X, Y, Z locations. This velocity was chosen to use for firebrand initial velocity in the following trials of prescribed fire simulation.

After finding the firebrands initial velocity (and the ejecting angle), the generation rate adjustments were carried out. The TH, TI, TJ, TK cases show the effect of varying the generation rate of firebrands for the firebrand flux on collection centers. The generation number increment/decrement was done by varying the number of firebrands in each firebrand size class that results in the adjustment to the total number as well. If the increment was mainly done for smaller firebrand classes (e.g., $0.75\text{--}5 \times 10^{-5} \text{ m}^2$), as we

could see more firebrands landing on Y, X locations in the succeeding run. It indicates smaller firebrands transport more distance from the fireline and larger firebrands land closer to it.

In contrast to the single tree burning simulation, the firebrand generation rate of a particular trial was kept constant with the constant HRRPUA of the prescribed fire. Figure 13a shows an example case of the accumulated total generated number of firebrands as time progressed. The same composition of firebrands according to size classes (e.g., 80% of $0.75\text{--}5 \times 10^{-5} \text{ m}^2$ and 6.2% of $50\text{--}10 \times 10^{-5} \text{ m}^2$) were maintained in every generation batch. Figure 13b shows almost the same number of firebrands landed at collection centers every second. The gradients of these plots are nearly constant after sometimes (40 s) which implies the firebrand fluxes keep nearly constant with time. Figure 13c,d illustrate this constant landing behavior for the size classes and shapes of the firebrands also.

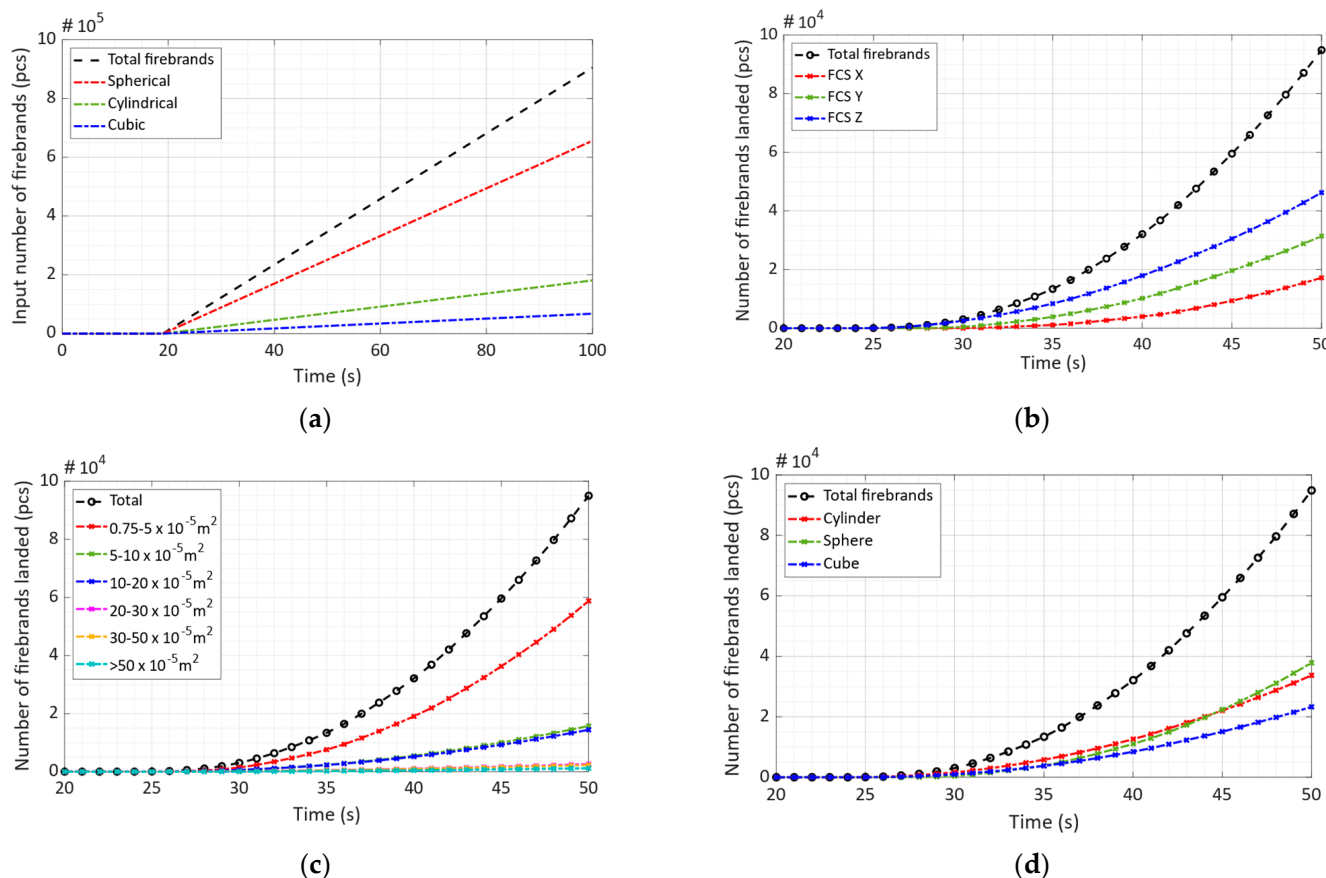


Figure 13. (a) The inputting/injecting number of firebrands against the time in terms of shapes and the total number. The injecting rate is kept constant. (b–d) The number of firebrands landed on the collection centers according to their landing locations, size classes, and shapes respectively. The landing rates of firebrands in these three representations are almost constant after some time (around 40 s).

The inverse analysis shows that the TK case is reasonably matched with the experiment. The firebrand flux difference at X, Y, Z locations is -2.0% , 16.7% , and 5.3% respectively. The total number of firebrands collected in the experiment is 1334 pcs and the simulation is 1499 pcs where the difference is $+10.9\%$. The percentage of collected firebrands to the total number of injected firebrands is around 6.7%. The estimated firebrand density (pcs/m²) at Z, Y, X locations in the simulation and the collected firebrand density in the field experiment are presented in Table 9.

The number of firebrands and the firebrand fluxes of individual size classes were calculated in each collection site. Figure 14 presents the size distribution of firebrands at

these locations for firebrand flux and number density against the firebrand size classes. The highest firebrand flux and number density were obtained by the smallest firebrand size class ($0.75\text{--}5 \times 10^{-5} \text{ m}^2$) on all three-firebrand collection centers. The nearest FCS Z (to the fireline) has the highest flux and number density while the furthest FCS X has the lowest. When the firebrand size increases, the distance of travel is decreased for all most every firebrand class. This behavior has slightly changed in the size classes of ($30\text{--}50 \times 10^{-5} \text{ m}^2$) at the Z location. There is a significant difference of over 70% in firebrand flux between the smallest and second smallest firebrand size classes in every collection center. Most injected firebrands consist of smaller size ($0.75\text{--}5 \times 10^{-5} \text{ m}^2$) firebrands could be a reason for this trend. Moreover, the difficulty of carrying larger firebrands to distances by the wind and the fire-buoyancy could be another reason for this. The firebrand flux and number density at the smallest size class are overestimated compared to the field experiment in all three locations. Having overestimated firebrand flux and number density at Z, Y location for larger firebrands (e.g., $20\text{--}30 \times 10^{-5} \text{ m}^2$, $30\text{--}50 \times 10^{-5} \text{ m}^2$, and $>50 \times 10^{-5} \text{ m}^2$) indicates the difficulty of carrying relatively large firebrands in downstream by the wind. This is confirmed by the underestimation of the flux and the density at X location for larger firebrands. The fire intensity can be a crucial reason for the instant nature of the wind field and the fire buoyancy which could be an effect on the firebrand generation and subsequent dynamics.

Table 9. The firebrand density of the experiment and simulation.

Location	FCS Z	FCS Y	FC X
Time span (s)	394	513	407
Firebrand density—experiment (pcs/m ²)	536	463	335
Firebrand density—simulation (pcs/m ²)	652	555	292

Overall, the above results show trends of firebrand landing flux, number density, and size distribution, a good agreement with the experiment. According to Figure 15a, the experimental and simulation results for total firebrand flux follow a similar trend only with a 13% difference at the smallest firebrand size class. Figure 15b illustrates the HRR and MLR of the case TK. The average heat release rate (HRR) of the fire is around 2672 MW and this would be continued because of the constant fire intensity of the fire. The total firebrand injection rate at that time is 11 171 pcs/s. Therefore, the firebrand generation rate is 4.18 pcs/MW/s or pcs/MJ where this value is 23% greater than the single tree burning simulation. The found firebrand generation rate is related to a specific Pine species at a certain wind velocity and FMC. To use these findings as firebrand generation source terms in any numerical modeling, we need to find the effects of species, wind, and FMC for firebrand generation rate according to the considering fire event.

These findings are used to investigate the firebrand generation rates for different kinds of pine species under the influence of wind, fuel moisture content, etc., with the outcomes of some field and laboratory experiments.

3.3. Quantifying the Effect of Wind, Vegetation Species, and Fuel Moisture Content for Firebrand Generation Rate

The effects of wind speed, fuel moisture content, and vegetation species to the firebrand generation rates are still not considered in the Section 3.2. Some experimental studies [6,9,14] showed that firebrand generation varies with these effects. To include influence of these parameters, we have interpolated the experimental results of Hudson et al. [6] and Bahrani et al. [14] to account them in the following subsections. The vegetation species of pitch pine, average wind velocity of 2 m/s, FMC of 31% in the prescribed forest fire and calculated firebrand generation rate of 4.18 pcs/MW/s are used as references to quantify these effects on firebrand generation rate for similar vegetation species in different wind speeds and FMCs.

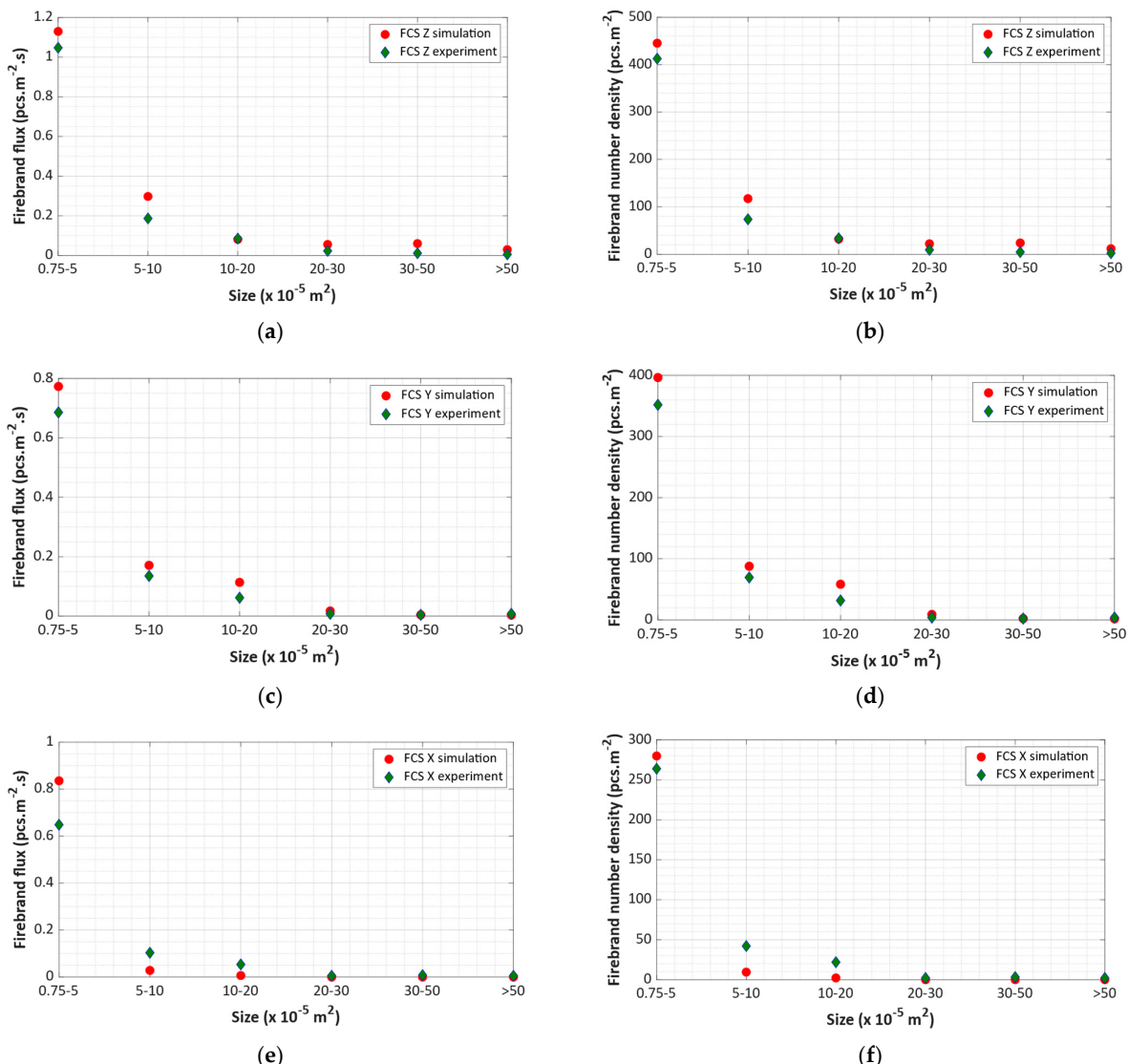


Figure 14. Firebrand flux (a,c,e), and number density (b,d,f) according to the size classes at Z, Y, X. Increasing the size of firebrands shows a decrement in both firebrand flux and number density at all the collection sites.

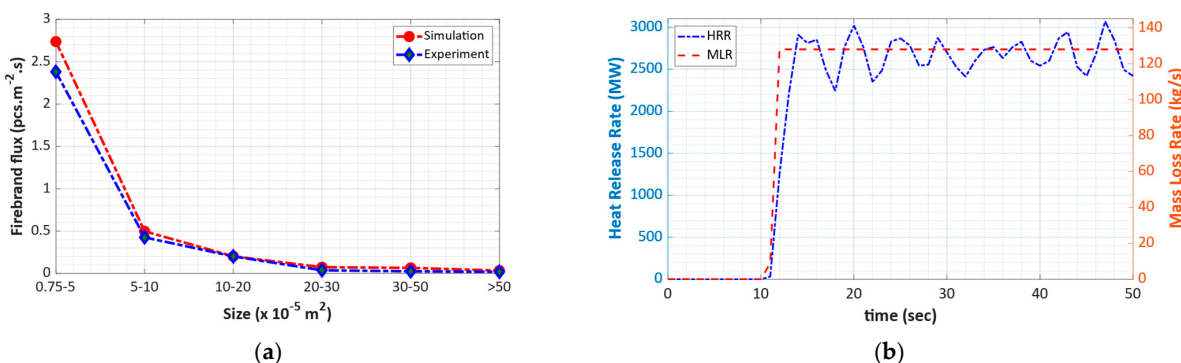


Figure 15. (a) Total firebrand flux comparison between the simulation and the experiment for size classes. (b) The heat release rate and mass-loss rate of the prescribed forest fire simulation for the first 50 s of the simulation. The fire has been started after 10 s and wind precursor was used to obtain the steady wind field.

3.3.1. Effect of the Vegetation Species for Firebrand Generation

The experiment of Hudson et al. [6] focused on the firebrand generation according to different fuel species such as Douglas Fir (DF), Grand Fir (GF), Ponderosa Pine (PP), and Western Juniper (*Juniperus occidentalis*) (WJ). Figure 16 illustrates the firebrand flux measured in this experiment and we assumed the landed firebrand flux is proportional to the firebrand generation rate as per Table 6. Therefore, it is reasonable to estimate the ratio of firebrand generation among species, according to the number of firebrands collected.

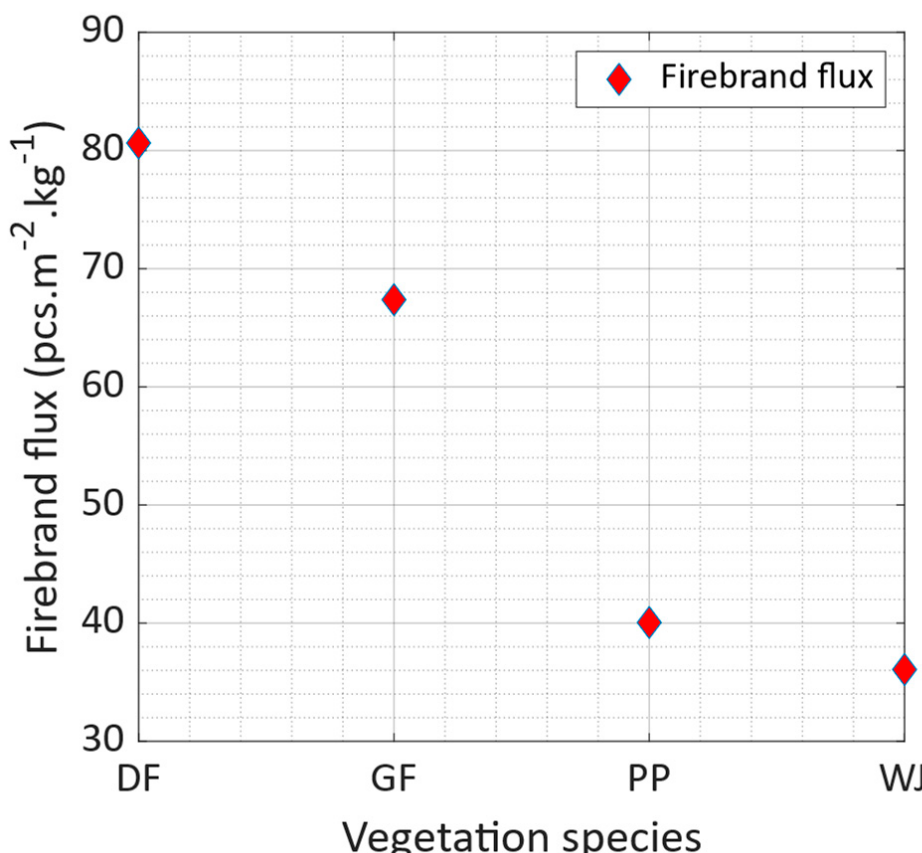


Figure 16. Firebrand flux per kilogram of fuel consumption of Douglas Fir (DF), Grand Fir (GF), Ponderosa Pine (PP), and Western Juniper (WJ) vegetation species [6].

Due to the scarcity of data, we assumed the similar pine species such as ponderosa pine and pitch pine produce the same number of firebrands at the same wind and fuel moisture conditions. From that, the firebrand generation ratios for given species were estimated relative to ponderosa pine as 2.01, 1.68, and 0.90 for DF/PP, GF/PP, and WJ/PP respectively. In other words, these ratios are considered as same as with the pitch pine. Therefore, in the same wind and FMC, the firebrand generation rates of Douglas fir, grand fir and western juniper will be $2.01 \times 4.18 \text{ pcs/MW/s}$, $1.68 \times 4.18 \text{ pcs/MW/s}$, and $0.9 \times 4.18 \text{ pcs/MW/s}$ respectively under a reference velocity of 2 m/s and FMC of 31%.

3.3.2. Effect of the Wind Speed for Firebrand Generation

According to Bahrani et al. [14], the number of firebrands generated from a particular fuel type varies with the wind speed. Therefore, accounting for the effect of wind speed on firebrand generation is important. In these experiments they investigated the wind effect for the firebrand generation of little bluestem grass (*Schizachyrium scoparium*), saw palmetto (*Serenoa repens*), chamise (*Adenostoma fasciculatum*), loblolly pine, and Leyland cypress. They have applied three different wind speeds (lower, medium and high) and collected all the firebrands generated from the tree burnings [14]. We assume Loblolly Pine

(LP) closely matches with pitch pine as they are from the same family and having similar physical appearance such as height, Diameter at Breast Height (DBH), crown area, bark thickness etc. [37]. We also present Leyland Cypress (LC) firebrand generation number in different wind velocities in Figure 17 [14] to show that the variation of firebrand generation for different species even in the same wind speed. The trendline for each data set and the equations are also displayed.

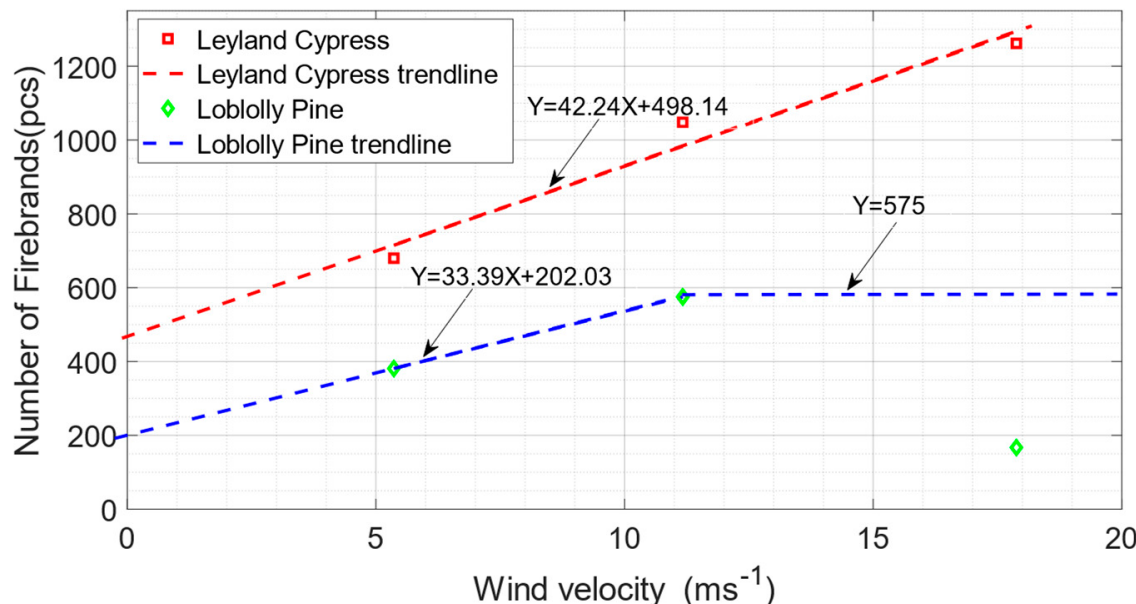


Figure 17. The experimental results of the number of firebrands collected at different wind speeds for loblolly pine and Leyland cypress vegetations. The experiment was conducted to collect all the firebrands generated in each tree burning [14].

In the experiment, the generated number of firebrands increase from lower to the higher wind for all the vegetation species except Loblolly pine. Therefore, for modeling purposes, we propose a trend of loblolly pine to remain the number of firebrands generation same in from medium wind condition assuming that the firebrand generation does not decrease with the wind. Placing the reference firebrand generation rate at 2 m/s on the trendline equations, we can estimate the number of firebrands generation at other wind velocities for specific species. This can be useful to approximate the number of firebrands generation in different severities of wildfires, explained for different jurisdictions such as Forest Fire Danger Index in Australia, Fire Weather Index (FWI) in Canada, National Fire Danger Rating System (NFDRS) in the USA that vary with the wind speed [38].

For example, the numeric value of FFDI can be varied from 50, 80, 100 according to the wind velocities of 11.1, 16.6 and 19.4 m/s when the other parameters such as environmental temperature, relative humidity and drought factor are constants. As per the trendline equations, the generation number of firebrands can be adjusted for these wind speeds.

3.3.3. Effect of Fuel Moisture Content for Firebrand Generation

In the experiments of Hudson et al. [6], firebrands were collected from burning western juniper and ponderosa pine trees at different FMCs. Figure 18 illustrates the number of firebrands generated in each tree species with different fuel moistures. As pitch pine and the ponderosa pine are closer vegetation species in terms of height, the shape of the canopy, etc., we can estimate the number of firebrands generation of ponderosa pine (considering equivalent to pitch pine) for different FMCs placing the reference firebrand generation rate with FMC 31% on the trendline equation. To do that, we use the PP-trendline equation given in Figure 18.

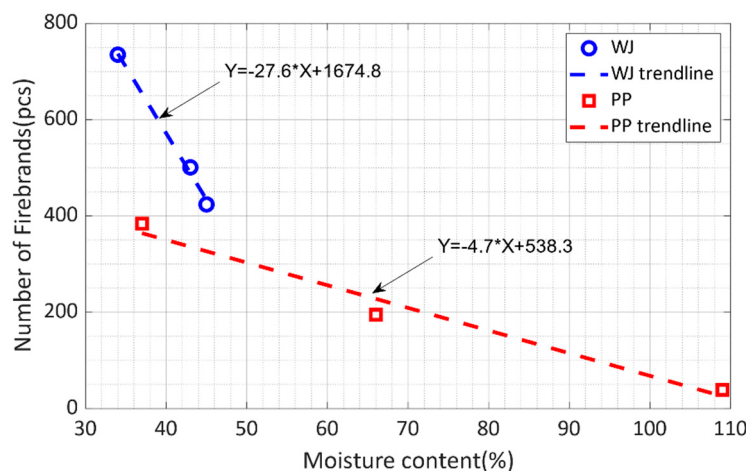


Figure 18. The number of firebrands generated varies the Fuel Moisture Content (FMC) of Western Juniper (WJ) and Ponderosa Pine (PP). Increasing FMC results decreasing in firebrand generation. The trend is linear, and it displays the equation of each trendline to find the number of firebrands generations in known FMC.

In wildland fire dynamics, the parameters such as wind, fuel species, and moisture content play a dominant role in the growth and spread of fires [39]. Similarly, the firebrand generation also depends on these parameters, which is shown in the experimental studies [6,7,14]. Moreover, the effects of these parameters are difficult to isolate from each other for firebrand generation in the complex turbulent flow fields associated with wind or buoyancy driven plumes. However, for 1% of FMC increment, western juniper and ponderosa pine vegetations show 1.72% and 1.34% decrement of the number of firebrands generation in the experiment of Hudson et al. [6]. In contrast to that Leyland cypress and loblolly pine vegetations show 0.65% and 0.48% increment of the number of firebrands generation for 1% of increment of wind speed according to Bahrani et al. [14] experiment. Although Douglas fir, grand fir, and ponderosa pine trees are conifers and come from same family (Pinaceae), the number of firebrands generation has a 16% and 50% difference in grand fir and ponderosa pine compared to Douglas fir as per Hudson et al. [6]. Under these circumstances, the importance of these parameters in contrast to each other is worth examining.

4. Conclusions and Future Works

In this study, a reliable methodology for determining firebrand generation using experimental data and physics-based simulation technique is presented. Once the firebrand generation rate is known, a wildfire operational model can be developed with inclusion of a spot fire feature. This will help to assess the risk of wildfires in an operational context. In the present work, the firebrand generation rate was correlated to the fire intensity by reproducing the firebrand landing distribution of a single tree burning and a prescribed forest fire experiments using the inverse analysis technique. For this, a well-validated physics-based model, FDS, is used. The firebrand landing distribution/collection data is reproduced by FDS by inputting the firebrand generation rate and initial velocities by trial and error. The thermophysical properties of the vegetation were taken from the literature. The fuel loads, firebrand data, environmental factors, and the fire intensity were similar to replicate the experimental conditions. For simulations, grid convergence was ensured through graphically as well as Grid Convergence Index (GCI). Performing the inverse analysis process, it was found the firebrand generation rate as 3.22 pcs/MW/s from the single Douglas fir tree burning and 4.18 pcs/MW/s in a pitch pine forest fire. It was shown that these values could be further calibrated with the variation of vegetation species, wind, and the Fuel Moisture Content (FMC) from several fields and laboratory experiments. Overall, the findings are expected to use to map firebrand flux and heat load on houses in

wildland urban interface as well as landing distribution on vegetation to assess the wildfire risk in future.

Author Contributions: Conceptualization, K.M. and A.W.; methodology, K.M. and A.W.; software, A.W.; validation, A.W.; formal analysis, A.W., K.M. and N.K.; investigation, A.W.; resources, K.M.; data curation, A.W.; writing—original draft preparation, A.W.; writing—review and editing, N.K. and K.M.; visualization, A.W.; supervision, K.M. and N.K.; project administration, K.M.; funding acquisition, K.M. All authors have read and agreed to the published version of the manuscript.

Funding: This research was funded by Bushfire and Natural Hazards CRC and the APC was funded by Victoria University.

Institutional Review Board Statement: Not applicable.

Informed Consent Statement: Not applicable.

Data Availability Statement: Not applicable.

Acknowledgments: We would like to acknowledge Bushfire and Natural Hazard Cooperative Research Centre for the financial support given. We are indebted to Samuel Manzello at NIST for providing Douglas fir tree burning and firebrand experimental data. The authors wish to thank Alexander Filkov for providing data on the prescribed forest burning field experiment conducted in PNR, and the insights were given to conduct the simulations.

Conflicts of Interest: The authors declare no conflict of interest.

References

- Blanchi, R.; Leonard, J.E.; Leicester, R.H. Lessons learnt from post-bushfire surveys at the urban interface in Australia. *For. Ecol. Manag.* **2006**, *234*, S139. [[CrossRef](#)]
- Muraszew, A.; Fedele, J.; Kuby, W. *Investigation of Fire Whirls and Firebrands*; Northern Forest Fire Laboratory, Intermountain Forest and Range Experiment: Missoula, MT, USA, 1976.
- Viegas, D.X.; Almeida, M.F.; Ribeiro, L.M. *Complexo de Incendios de Pedrógão Grande e Concelhos Limítrofes Limítrofes*; University of Coimbra: Coimbra, Portugal, 2017.
- Sharifian, A.; Hashempour, J. A novel ember shower simulator for assessing performance of low porosity screens at high wind speeds against firebrand attacks. *J. Fire Sci.* **2016**, *34*, 335–355. [[CrossRef](#)]
- Leonard, J.; Blanchi, R.; Bowditch, P. Bushfire impact from a house's perspective. In Proceedings of the Earth Wind and Fire–Bushfire 2004 Conference, Adelaide, Australia, 25–28 May 2004.
- Hudson, T.R.; Bray, R.B.; Blunck, D.L.; Page, W.; Butler, B. Effects of fuel morphology on ember generation characteristics at the tree scale. *Int. J. Wildland Fire* **2020**, *29*, 1042–1051. [[CrossRef](#)]
- Adusumilli, S.; Hudson, T.; Gardner, N.; Blunck, D.L. Quantifying production of hot firebrands using a fire-resistant fabric. *Int. J. Wildland Fire* **2021**, *30*, 154–159. [[CrossRef](#)]
- Filkov, A.; Prohanov, S.; Mueller, E.; Kasymov, D.; Martynov, P.; El Houssami, M.; Thomas, J.; Skowronski, N.; Butler, B.; Gallagher, M. Investigation of firebrand production during prescribed fires conducted in a pine forest. *Proc. Combust. Inst.* **2017**, *36*, 3263–3270. [[CrossRef](#)]
- Manzello, S.L.; Maranghides, A.; Mell, W.E. Firebrand generation from burning vegetation. *Int. J. Wildland Fire* **2007**, *16*, 458–462. [[CrossRef](#)]
- El Houssami, M.; Mueller, E.; Filkov, A.; Thomas, J.C.; Skowronski, N.; Gallagher, M.R.; Clark, K.; Kremens, R.; Simeoni, A. Experimental procedures characterising firebrand generation in wildland fires. *Fire Technol.* **2016**, *52*, 731–751. [[CrossRef](#)]
- Manzello, S.L.; Maranghides, A.; Shields, J.R.; Mell, W.E.; Hayashi, Y.; Nii, D. Measurement of firebrand production and heat release rate (HRR) from burning Korean pine trees. *Fire Saf. Sci.* **2007**, *7*, 108.
- Filkov, A.; Kasymov, D.; Zima, V.; Matvienko, O. Experimental investigation of surface litter ignition by bark firebrands. In Proceedings of the AIP Conference Proceedings, Tomsk, Russia, 15 January 2016; p. 060004.
- Filkov, A.; Prohanov, S. Particle Tracking and Detection Software for Firebrands Characterization in Wildland Fires. *Fire Technol.* **2019**, *55*, 817–836. [[CrossRef](#)]
- Bahrani, B. *Characterization of Firebrands Generated from Selected Vegetative Fuels in Wildland Fires*; The University of North Carolina at Charlotte: Charlotte, NC, USA, 2020.
- Wadhwan, R. *Physics-Based Simulation of Short-Range Spotting in Wildfires*; Victoria University: Victoria, BC, Canada, 2019.
- Haider, A.; Levenspiel, O. Drag coefficient and terminal velocity of spherical and nonspherical particles. *Powder Technol.* **1989**, *58*, 63–70. [[CrossRef](#)]
- McDermott, R.; McGrattan, K.; Hostikka, S. *Fire Dynamics Simulator (Version 5) Technical Reference Guide*; National Institute of Standards and Technology NIST: Gaithersburg, MD, USA, 2008; Volume 1018.

18. Moinuddin, K.; Sutherland, D. Modelling of tree fires and fires transitioning from the forest floor to the canopy with a physics-based model. *Math. Comput. Simul.* **2019**, *175*, 81–95. [[CrossRef](#)]
19. Sarwar, M.; Cleary, M.; Moinuddin, K.; Thorpe, G.R.; Flow, F. On linking the filter width to the boundary layer thickness in explicitly filtered large eddy simulations of wall bounded flows. *Int. J. Heat Fluid Flow* **2017**, *65*, 73–89. [[CrossRef](#)]
20. McGrattan, K.; Klein, B.; Hostikka, S.; Floyd, J. *Fire Dynamics Simulator (Version 5), User's Guide*; National Institute of Standards and Technology NIST: Gaithersburg, MD, USA, 2010; Volume 1019, pp. 1–186.
21. McGrattan, K.B.; Baum, H.R.; Rehm, R.G.; Hamins, A.; Forney, G.P.; Floyd, J.E.; Hostikka, S.; Prasad, K. *Fire Dynamics Simulator-Technical Reference Guide*; National Institute of Standards and Technology, Building and Fire Research: Gaithersburg, MD, USA, 2000.
22. Ali, M.S.M.; Doolan, C.J.; Wheatley, V. Grid convergence study for a two-dimensional simulation of flow around a square cylinder at a low Reynolds number. In *School of Mechanical & Mining Engineering Publications, Proceedings of the Seventh International Conference on CFD in The Minerals and Process Industries, Melbourne, Australia, 9–11 December 2009*; Witt, P.J., Schwarz, M.P., Eds.; CSIRO: Melbourne, Australia, 2009; pp. 1–6.
23. Roy, C.J. Grid convergence error analysis for mixed-order numerical schemes. *AIAA J.* **2003**, *41*, 595–604. [[CrossRef](#)]
24. Mell, W.; Maranghides, A.; McDermott, R.; Manzello, S.L. Numerical simulation and experiments of burning douglas fir trees. *Combust. Flame* **2009**, *156*, 2023–2041. [[CrossRef](#)]
25. Technology, NISOA. Available online: https://github.com/firemodels/fds/blob/master/Validation/NIST_Douglas_Firs/FDS_Input_Files/tree_2_m_14_pc.fds (accessed on 12 December 2019).
26. Forney, G.P. *Smokeview (Version 5)-A Tool for Visualizing Fire Dynamics Simulation Data, Volume I: User's Guide*; National Institute of Standards and Technology: Gaithersburg, MD, USA, 2017.
27. Manzello, S.L.; Maranghides, A.; Shields, J.R.; Mell, W.E.; Hayashi, Y.; Nii, D. Mass and size distribution of firebrands generated from burning Korean pine (*Pinus koraiensis*) trees. *Fire Mater.* **2009**, *33*, 21–31. [[CrossRef](#)]
28. Thomas, J.C.; Mueller, E.V.; Santamaria, S.; Gallagher, M.; El Houssami, M.; Filkov, A.; Clark, K.; Skowronski, N.; Hadden, R.M.; Mell, W. Investigation of firebrand generation from an experimental fire: Development of a reliable data collection methodology. *Fire Saf. J.* **2017**, *91*, 864–871. [[CrossRef](#)]
29. Baker, E.S. *Burning Characteristics of Individual Douglas-Fir Trees in the Wildland/Urban Interface*; Worcester Polytechnic Institute: Worcester, MA, USA, 2011.
30. Alexander, M.E.; Cruz, M.G. Interdependencies between flame length and fireline intensity in predicting crown fire initiation and crown scorch height. *Int. J. Wildland Fire* **2011**, *21*, 95–113. [[CrossRef](#)]
31. Jarrin, N.; Benhamadouche, S.; Laurence, D.; Prosser, R. A synthetic-eddy-method for generating inflow conditions for large-eddy simulations. *Int. J. Heat Fluid Flow* **2006**, *27*, 585–593. [[CrossRef](#)]
32. Muller-Landau, H.C.; Wright, S.J.; Calderón, O.; Condit, R.; Hubbell, S.P. Interspecific variation in primary seed dispersal in a tropical forest. *J. Ecol.* **2008**, *96*, 653–667. [[CrossRef](#)]
33. Mitsopoulos, I.D.; Dimitrakopoulos, A. Canopy fuel characteristics and potential crown fire behavior in Aleppo pine (*Pinus halepensis* Mill.) forests. *Ann. For. Sci.* **2007**, *64*, 287–299. [[CrossRef](#)]
34. Mueller, E.V. Examination of the Underlying Physics in a Detailed Wildland Fire Behavior Model through Field-Scale Experimentation. Ph.D. Thesis, The University of Edinburgh, Edinburgh, UK, 2017.
35. Menzemer, L.W. Numerical Simulations of Brand Transport in Large Outdoor Fires. Master's Thesis, Ghent University, Ghent, Belgium, 2021.
36. Khan, N.; Moinuddin, K.J.A. The Role of Heat Flux in an Idealised Firebreak Built in Surface and Crown Fires. *Atmosphere* **2021**, *12*, 1395. [[CrossRef](#)]
37. Dipesh, K.; Will, R.E.; Lynch, T.B.; Heinemann, R.; Holeman, R.J.F.S. Comparison of loblolly, shortleaf, and pitch X loblolly pine plantations growing in Oklahoma. *For. Sci.* **2015**, *61*, 540–547. [[CrossRef](#)]
38. Matthews, S.J.A.M.; Journal, O. A comparison of fire danger rating systems for use in forests. *Aust. Meteorol. Oceanogr. J.* **2009**, *58*, 41. [[CrossRef](#)]
39. Moinuddin, K.; Khan, N.; Sutherland, D. Numerical study on effect of relative humidity (and fuel moisture) on modes of grassfire propagation. *Fire Saf. J.* **2021**, *125*, 103422. [[CrossRef](#)]